ACCSCIENCE PUBLISHING

Journal of Seismic Exploration

ARTICLE

Sparse multi-channel simultaneous seismic impedance inversion in the Laplace–Fourier domain for well-free low-frequency recovery

Guangzhao Guo[1], Kai Lin[1]*, Yuqiang Zhang[1], Xiaotao Wen[1], and Lian Zhao[2]

[1]The Key Laboratory of Earth Exploration and Information Techniques, School of Geophysics, Chengdu University of Technology, Chengdu, Sichuan, China

[2]The State Key Laboratory of Deep Oil and Gas, School of Geosciences, China University of Petroleum (East China), Qingdao, Shandong, China

Abstract

Seismic acoustic impedance (AI) inversion is fundamentally ill-posed due to the band-limited nature of recorded seismic wavefields. In frontier exploration areas lacking reliable well controls, establishing an accurate low-frequency background model (typically 0–10 Hz) is difficult. Furthermore, conventional trace-by-trace inversion schemes neglect lateral spatial correlations, rendering results highly sensitive to random noise and disruptive to stratigraphic continuity. To simultaneously overcome these dual limitations, we propose a novel multi-channel simultaneous inversion framework that integrates deterministic sparse regularization with the Laplace–Fourier domain. Unlike conventional methods that rely on well-log interpolation for low-frequency compensation, our approach estimates low-frequency AI trends from band-limited seismic data through Laplace damping, subject to wavelet calibration and the adopted background-scale constraints. Concurrently, multi-channel structural constraints are imposed via total variation regularization to preserve sharp lithological boundaries and enforce lateral continuity across adjacent traces. The resulting large-scale multi-trace AI optimization problem is solved efficiently using the alternating direction method of multipliers coupled with a two-dimensional Sylvester equation, bypassing the need to store massive sparse coefficient matrices. Comprehensive tests on synthetic data—with explicitly high-pass filtered inputs—and field data demonstrate that the proposed method estimates the 0–10 Hz background trend without a spatially interpolated well-log model under the adopted initialization and calibration assumptions, improves lateral continuity and the delineation of impedance contrasts and stratigraphic boundaries in the tested examples, and exhibits superior noise robustness compared to conventional linear baselines.

Keywords: Laplace–Fourier domain; Multi-channel inversion; Acoustic impedance inversion; Alternating direction method of multipliers

***Corresponding author:**
Kai Lin
(linkai13@cdut.cn)

Citation: Guo G, Lin K, Zhang Y, Wen X, Zhao L. Sparse multi-channel simultaneous seismic impedance inversion in the Laplace–Fourier domain for well-free low-frequency recovery. *J Seismic Explor*. doi: 10.36922/JSE026330152

Received: August 12, 2026

Revised: October 20, 2026

Accepted: November 2, 2026

Published online: November 20, 2026

Copyright: © 2026 Author(s). This is an Open-Access article distributed under the terms of the Creative Commons Attribution License, permitting distribution, and reproduction in any medium, provided the original work is properly cited.

Publisher's Note: AccScience Publishing remains neutral with regard to jurisdictional claims in published maps and institutional affiliations.

1. Introduction

Seismic acoustic impedance (AI) inversion serves as a critical bridge connecting seismic wavefields to quantitative reservoir parameters. By transforming relative reflection

boundaries into absolute layer-property attributes, this parameter effectively characterizes subsurface lithology.[1] However, conventional post-stack inversion methods for estimating AI are heavily dependent on a priori low-frequency models. A reliable low-frequency model is required to provide the long-wavelength background structures missing from the band-limited seismic data.[2] In exploration regions with sparse or no well control, establishing an accurate low-frequency background via well-log interpolation is unfeasible. Although significant progress has been made in broadening seismic acquisition bandwidth and optimizing inversion regularization terms, this dependency on a priori low-frequency models remains a critical algorithmic bottleneck in seismic inversion.[3-8] From a petrophysical perspective, the absence of these low-frequency components (typically 0–10 Hz) prevents the transformation of relative reflectivity into absolute AI. This limitation is particularly critical for quantitative reservoir characterization, as the low-frequency background trend contains essential information regarding the burial history and compaction of sedimentary sequences. Without an accurate recovery of this long-wavelength information, the inversion results may fail to differentiate between lithological variations and fluid-driven anomalies, thereby increasing the risk in sweet-spot prediction.[9-11]

Recorded reflection seismic data have a finite usable bandwidth and therefore do not directly constrain very low- or very high-frequency components. Conventional conversion of reflectivity to absolute AI supplements the missing long-wavelength background with low-frequency information commonly derived from well logs. When well coverage is incomplete, the proposed method can estimate a low-frequency AI trend from the available seismic data without requiring a spatially interpolated well-log background. This does not remove the need for a calibrated wavelet and a justified background scale or weak prior: the estimate remains conditional on these assumptions rather than a unique recovery of unmeasured frequencies. Thus, applicability with limited well coverage should not be interpreted as completely independent estimation of absolute AI without any prior information.

To overcome the critical dependence on an a priori low-frequency background model, significant research efforts have focused on directly retrieving low-frequency content from band-limited seismic wavefields through envelope inversion or techniques in the Laplace–Fourier domain (LFD). Shin and Cha[12,13] exploited the zero-frequency response of damped wavefields in Laplace-domain and LFD full waveform inversion to estimate long-wavelength model components. To reduce the sensitivity to damping constants, subsequent studies introduced multiple frequency components and damping strategies to construct refined velocity models.[12-16] Transitioning to the domain of impedance inversion, Li *et al.*[2] advanced a Bayesian scheme formulated specifically within the Laplace mixed-domain. Similarly, Li *et al.*[17] derived a stationary convolution operator and constructed an objective functional based on Bayesian maximum a posteriori estimation, demonstrating potential for low-frequency estimation. Following these pioneering works, most LFD-based approaches have relied on the Bayesian statistical framework, applying probabilistic priors to estimate elastic parameters in nonlinear inversion or anisotropic media.[18-21] The physical mechanism of low-frequency recovery in the LFD stems from the asymmetric time-domain weighting induced by the damping operator. For a conventional band-limited seismic wavelet lacking zero-frequency energy, its standard Fourier spectrum intrinsically maintains a zero-mean property due to symmetric positive and negative amplitude cancellations. By introducing a Laplace frequency with a positive damping constant, the Laplace transform applies a monotonically decaying exponential time window to the seismic record. This asymmetric damping breaks the waveform symmetry and disrupts the exact amplitude cancellation of the original band-limited wavelet, forcing non-zero energy projections into the zero- and ultra-low-frequency bands. These damped spectral components can constrain an estimate of the long-wavelength AI trend without spatial well-log interpolation; they do not supply independent observations of frequencies absent from the recorded data.

Bayesian estimates depend on their likelihood and priors. Gaussian quadratic priors can smooth sharp stratigraphic boundaries, whereas sparsity-promoting priors can preserve sharper transitions; excessive smoothing is not an inherent property of Bayesian inference. In contrast, deterministic sparse regularization offers a powerful alternative by directly imposing sparsity constraints on the reflectivity. Tikhonov regularization, based on the L_2 norm, reduces ill-posedness but limits resolution.[22,23] Propelled by advancements in compressive sensing, sparse regularization strategies utilizing L_1 norm or L_p norm ($0 < p < 1$) have garnered considerable interest, primarily for their capability to yield "blocky" inversion profiles featuring distinct high-resolution interfaces.[24-27] However, these sparse regularization techniques are predominantly applied in the conventional time or frequency domains and have rarely been integrated with the low-frequency mining capabilities of the LFD. Unlike the L_2 norm, which penalizes large residuals quadratically and results in blurred interfaces, the L_1 norm or total variation-based constraints allow for the existence of sparse, high-amplitude reflection coefficients. Mathematically, this corresponds to the

"heavy-tailed" distribution often observed in well-log data. By enforcing such constraints, the inversion can better honor sharp discontinuities at geological boundaries—such as unconformities or fault planes—ensuring that the recovered impedance profiles retain high-frequency detail even when the seismic bandwidth is limited.[28]

Furthermore, traditional inversion methods often operate trace by trace, inadvertently treating neighboring traces as independent and neglecting the intrinsic lateral spatial correlation of subsurface sedimentary structures. To mitigate this lateral inconsistency, total variation regularization and multi-channel constraints have been widely explored.[29-33] By utilizing lateral and vertical differential operators to penalize non-geological variations, these methods enforce structural continuity, which allows them to effectively suppress spatially incoherent random noise while rigorously preserving sharp lithological interfaces. However, integrating these robust multi-channel spatial constraints with the low-frequency recovery potential of the LFD strategy within a unified regularization framework remains an underexplored frontier.

Many existing LFD implementations use Bayesian trace-by-trace inversion. Their smoothness depends on the selected priors, while independent-trace processing does not explicitly enforce lateral spatial correlations. Addressing these limitations, this study proposes a novel multi-channel simultaneous inversion method based on sparse regularization in the LFD. Representing a paradigm shift from traditional Bayesian inference to a deterministic regularization framework, our approach innovatively integrates the low-frequency mining capability of the Laplace–Fourier transform with sparsity-promoting constraints. Unlike probabilistic methods, this framework directly utilizes sparse norms to estimate low-frequency AI trends without requiring a spatially interpolated well-log background while preserving sharp stratigraphic boundaries. Furthermore, by extending the inversion scheme from a single-channel to a multi-channel simultaneous framework, we enforce lateral spatial constraints to significantly suppress noise and enhance the continuity of geologic structures. To efficiently address the derived multi-trace AI optimization challenge, we integrate the alternating direction method of multipliers (ADMM) algorithm with the two-dimensional (2D) Sylvester equation, thereby guaranteeing the computational stability and feasibility required for large-scale seismic data processing. The transition from trace-by-trace to multi-channel simultaneous inversion inevitably leads to a massive increase in the dimensionality of the coefficient matrix, posing a significant challenge for computational efficiency. To address this "curse of dimensionality," we leverage the mathematical structure of the 2D Sylvester equation within the ADMM framework. By exploiting the separability of the lateral and vertical differential operators, the Sylvester equation enables a closed-form solution in the frequency domain.[34,35] This strategy bypasses the need for explicit storage of large, sparse matrices and drastically reduces the computational overhead, making the high-resolution multi-channel inversion feasible for large-scale three-dimensional (3D) seismic surveys.

In this study, simultaneous inversion refers to joint estimation of AI on neighboring seismic traces using shared lateral constraints. It does not denote simultaneous estimation of several elastic parameters. The forward model and the results discussed below concern post-stack AI inversion.

2. Mechanism of low-frequency recovery in the Laplace–Fourier domain

The LFD transform (Laplace transform) uses a series of complex exponential signals with different amplitudes and attenuation rates to reveal the frequency composition and transient characteristics of each component of the signal. For time-domain seismic signals $y(t)$, the LFD transformation can be expressed as simultaneously performing a Laplace transform on both sides of the equation $Y(s)$ (**Equation 1**):

$$Y(s)=\int_0^{+\infty} y(t)e^{-st}dt+N(s) \tag{1}$$

Among them, the Laplace frequency $s=\sigma+i\omega$ defines a continuous complex plane (s-plane), where σ and ω are damping factors and frequencies (**Equation 2**):

$$Y(s)=\int_0^{+\infty} y(t)e^{-\sigma t}e^{-i\omega t}dt+N(s) \tag{2}$$

The exponential factors in **Equation 2** apply mathematical damping and Fourier phase weighting, respectively. σ controls the decay of the time window, whereas $\omega=2\pi f$ is the angular frequency. This weighting is not a physical model of intrinsic seismic attenuation.

The blue curves in Figure 1 show the undamped wavelet and its synthetic seismic trace. The colored curves show these signals after exponential time weighting with different damping coefficients. The reduced contribution of later time samples is imposed by the transform kernel, not by a change in subsurface absorption.

Figure 2 presents the normalized amplitude spectra of the wavelet and synthetic seismic record in the complex-frequency domain, where zero damping corresponds to the conventional Fourier domain. As the damping coefficient increases, the mid- and high-frequency spectral amplitudes generally decrease. However, the low-frequency region

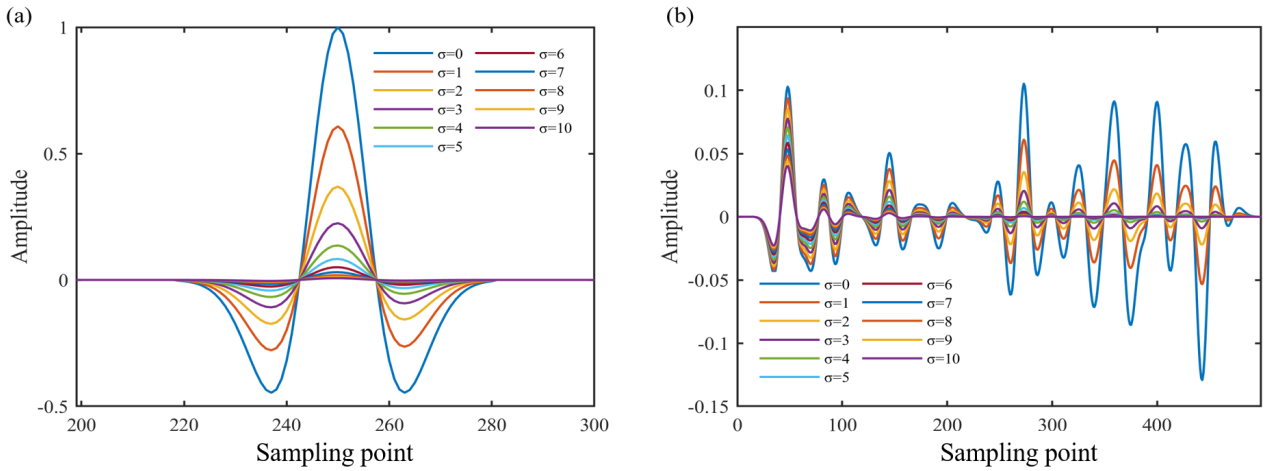


Figure 1. Effect of Laplace damping on (a) the wavelet and (b) the synthetic seismic trace. Curves correspond to the damping constants in the legends; blue denotes zero damping. The horizontal axes show sampling-point indices. The damping constant σ controls the exponential weighting of the wavelet and trace.

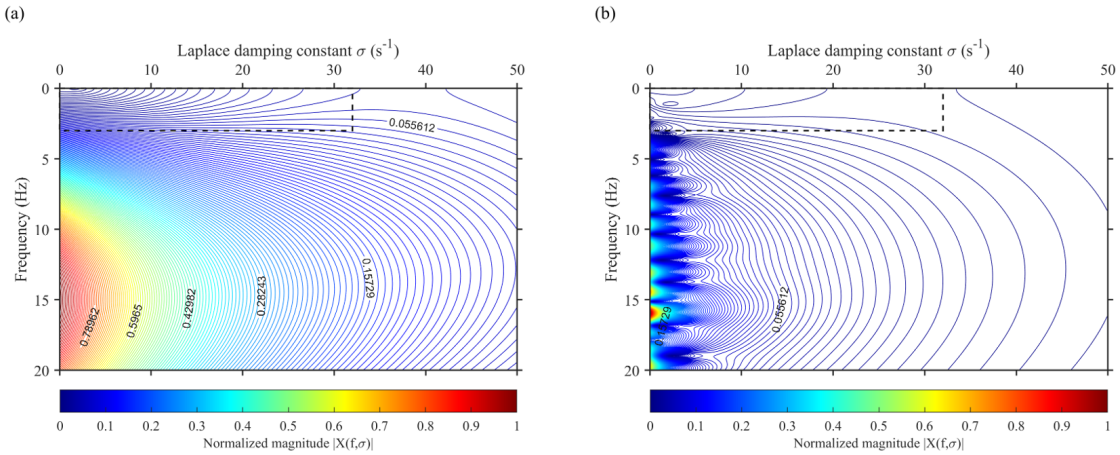


Figure 2. Normalized complex-frequency amplitude spectra of (a) the Ricker wavelet and (b) the synthetic seismic trace. Dashed boxes indicate the 0–3 Hz band; zero damping gives the Fourier spectrum. Colors and contours show normalized amplitude; the axes are the damping constant σ in s^{-1} and frequency in Hz.

(0–3 Hz), highlighted by the dashed boxes, exhibits a different response: some low-frequency components show local enhancement over certain damping ranges rather than decreasing monotonically, making initially weak low-frequency responses more apparent. Compared with the relatively smooth variations in the wavelet spectrum, the seismic spectrum exhibits more complex fluctuations under weak damping, which gradually diminish as damping increases.

These observations indicate that damping changes the contributions of different time samples to the spectrum and their cancellation relationships, thereby reshaping the low-frequency spectral response. This provides a basis for examining low-frequency constraints in complex-frequency-domain inversion. However, enhanced spectral amplitudes do not imply the introduction of additional independent low-frequency information. The accuracy and stability of low-frequency recovery must therefore be further assessed through inversion experiments that account for damping, frequency sampling, noise, and prior assumptions.

Figure 3 shows the spectral amplitudes of the wavelet and synthetic trace as functions of the damping coefficient σ at selected fixed frequencies. The response is frequency

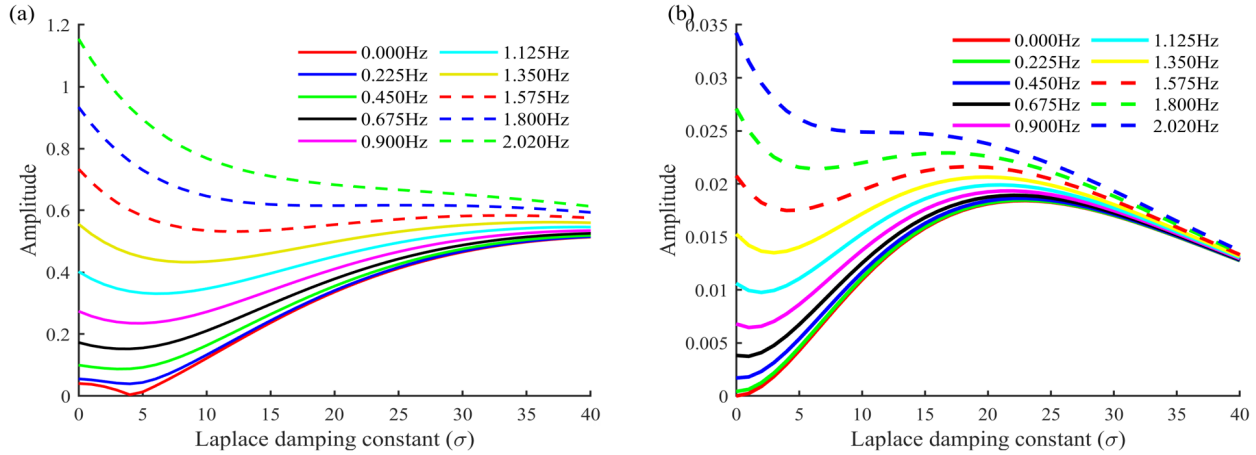


Figure 3. Spectral amplitude versus Laplace damping constant at selected frequencies from 0 to 2.020 Hz: (a) wavelet; (b) synthetic seismic trace. Each curve represents a fixed frequency, as listed in the legend. The horizontal axis is σ and the vertical axis is spectral amplitude.

dependent and is not generally monotonic: several curves rise over one damping interval and then decrease, while others change more weakly. A positive damping coefficient can produce a non-zero zero-frequency projection even when the undamped zero-frequency component vanishes, because exponential time weighting changes the cancellation between positive and negative waveform contributions. Its amplitude is not generally proportional to damping. This effect represents a deterministic reweighting of the recorded samples; it neither compensates for physical seismic attenuation nor creates independent observations in an unrecorded frequency band. The resulting low-frequency constraints therefore support a data- and prior-dependent background estimate, whose stability must be evaluated against damping, wavelet, noise, and regularization choices.

3. Seismic forward solver in the Laplace–Fourier domain

According to Robinson's convolution model, time-domain seismic signals can be represented as the convolution of seismic wavelets $\omega(t)$ and reflection coefficients $r(t)$ (**Equation 3**):

$$y(t)=\int_0^{+\infty}\omega(t-\tau)r(\tau)d\tau+n(t) \tag{3}$$

where $\omega(t-\tau)$ is the time-domain seismic wavelet with time constraints, and τ and is the integral variable.

Introducing Robinson's stationary convolution model (**Equation 3**) into **Equation 2** gives **Equation 4**:

$$\begin{aligned}Y(s)&=\int_0^{+\infty}\left[\int_0^{+\infty}\omega(t-\tau)r(\tau)d\tau\right]e^{-\sigma t}e^{-i\omega t}dt+N(s)\\&=\int_0^{+\infty}\left[\int_0^{+\infty}\omega(t-\tau)e^{-\sigma t}e^{-i\omega t}dt\right]r(\tau)d\tau+N(s)\end{aligned} \tag{4}$$

According to the time shift property of the Fourier transform, the time-domain convolution model can be transformed into an LFD equation; that is, **Equation 4** can be rewritten as **Equation 5**:

$$Y(s)=W(\sigma+i\omega)\int_0^{+\infty}r(\tau)e^{-\sigma\tau}e^{-i\omega\tau}d\tau+N(s) \tag{5}$$

where $W(\sigma+i\omega)$ is the complex spectrum of the time-domain seismic wavelet.

If given a specific frequency component, the LFD equation (**Equation 5**) can be expressed as the following matrix equation (**Equation 6**):

$$Y_{\omega_j}=W_{\omega_j}\cdot C\cdot E_{\omega_j}\cdot R+N_{\omega_j} \tag{6}$$

where W_{ω_j}, C, and E_{ω_j} represent the Laplace frequency spectrum of the seismic wavelet, the time-domain attenuation coefficient matrix of the LFD transformation, and the Fourier forward operator, respectively. Y_{ω_j} is the complex spectrum of seismic signals at a specific frequency ω_j, and R is the reflection coefficient. W_{ω_j}, C and E_{ω_j} can be expressed in matrix form (**Equations 7–9**):

$$W_{\omega_j}=\begin{bmatrix}W(\sigma_1+i\omega_j) & 0 & \cdots & 0\\ 0 & W(\sigma_2+i\omega_j)\cdots & & 0\\ \vdots & \vdots & \ddots & \vdots\\ 0 & 0 & \cdots W(\sigma_k+i\omega_j)\end{bmatrix}_{k*k} \tag{7}$$

$$C=\begin{bmatrix}e^{-\sigma_1\tau_1} & e^{-\sigma_1\tau_2}\cdots e^{-\sigma_1\tau_M}\\ e^{-\sigma_2\tau_1} & e^{-\sigma_2\tau_2}\cdots e^{-\sigma_2\tau_M}\\ \vdots & \vdots\ \ddots\ \vdots\\ e^{-\sigma_k\tau_1} & e^{-\sigma_k\tau_2}\cdots e^{-\sigma_k\tau_M}\end{bmatrix}_{k*M} \tag{8}$$

$$E_{\omega_j}=\begin{bmatrix}e^{-i\omega_j\tau_1} & 0 & \cdots & 0\\ 0 & e^{-i\omega_j\tau_2}\cdots & & 0\\ \vdots & \vdots & \ddots & \vdots\\ 0 & 0 & \cdots e^{-i\omega_j\tau_M}\end{bmatrix}_{M*M} \tag{9}$$

The reflection coefficient can be represented by AI (**Equation 10**):

$$R_i = \frac{Z_{i+1} - Z_i}{Z_{i+1} + Z_i} \approx \frac{1}{2}\Delta \ln Z_i$$
$$= \frac{1}{2}\left(\ln Z_{i+1} - \ln Z_i\right) = \frac{1}{2} D \ln Z_i \quad (10)$$

where Z represents AI, ln$Z$ represents the logarithm of AI, and D represents the first-order difference matrix.

Let $L = \ln Z$ and $D' = \frac{1}{2}D$, then **Equation 6** can be written as **Equation 11**:

$$Y_{\omega_j} = W_{\omega_j} \cdot C \cdot E_{\omega_j} \cdot D' \cdot L + N_{\omega_j} \quad (11)$$

Let k and l denote the number of damping coefficients and sampled frequencies, M the number of samples on the common transform grid, n the number of model samples per trace, and q the number of traces. Combining **Equations 6–9** gives **Equation 12**:

$$\underbrace{\begin{bmatrix} Y_{\omega_1} \\ Y_{\omega_2} \\ \vdots \\ Y_{\omega_l} \end{bmatrix}_{kl}}_{Y} = \underbrace{\begin{bmatrix} W_{\omega_1} \cdot C & 0 & \cdots & 0 \\ 0 & W_{\omega_2} \cdot C & \vdots & \vdots \\ \vdots & \vdots & \ddots & 0 \\ 0 & 0 & 0 & W_{\omega_l} \cdot C \end{bmatrix}_{kl \cdot Ml}}_{G} \underbrace{\begin{bmatrix} E_{\omega_1} \\ E_{\omega_2} \\ \vdots \\ E_{\omega_l} \end{bmatrix}_{Ml \cdot M}}_{E} \cdot D'L + \underbrace{\begin{bmatrix} N_{\omega_1} \\ N_{\omega_2} \\ \vdots \\ N_{\omega_l} \end{bmatrix}_{kl}}_{N} \quad (12)$$

Here, $Y, N \in \boldsymbol{C}^{kl \times q}$ contain the data and noise; each frequency block has k rows. The operators have dimensions $W_{\omega_j} \in \boldsymbol{C}^{k \times k}$, $C \in \boldsymbol{R}^{k \times M}$, $E_{\omega_j} \in \boldsymbol{C}^{M \times M}$, $E \in \boldsymbol{C}^{lM \times M}$, and $G \in \boldsymbol{C}^{kl \times lM}$. The matrix G is block diagonal in the frequency blocks $W_{\omega_j} C$, and E vertically stacks the phase matrices. **Equation 12** applies to one trace or to all q traces as columns. The complex equation is equivalently written in real form as **Equation 13**:

$$\begin{bmatrix} real(Y) \\ imag(Y) \end{bmatrix} = \begin{bmatrix} real(G \cdot E) \\ imag(G \cdot E) \end{bmatrix} \cdot D'L + \begin{bmatrix} real(N) \\ imag(N) \end{bmatrix} \quad (13)$$

For real model variables, define $Y' = vcat(\mathrm{Re}\,Y, ImY)$ and $N' = vcat(\mathrm{Re}\,N, ImN)$, where vcat denotes vertical concatenation with all real rows preceding all imaginary rows. Let $L' = vcat(\mathrm{Re}\,E, ImE)$. Define G' by the two block rows $[\mathrm{Re}\,G, -ImG]$ and $[ImG, \mathrm{Re}\,G]$, respectively. Then $G'L' = vcat(\mathrm{Re}(GE), Im(GE))$, and **Equation 13** becomes:

$$Y' = G' \cdot L' \cdot D' \cdot L + N' \quad (14)$$

The real arrays have dimensions $Y', N' \in \boldsymbol{R}^{2kl \times q}$, $G' \in \boldsymbol{R}^{2kl \times 2lM}$, and $L' \in \boldsymbol{R}^{2lM \times M}$. The log AI model and its background satisfy $L, L_0 \in \boldsymbol{R}^{n \times q}$. The first-difference operator $D \in \boldsymbol{R}^{M \times n}$ contains the adjacent differences of the model, with zero extension onto the transform grid where required, and $D' = 0.5D$. Thus the full real forward operator has size $2kl \times n$. Real and imaginary data blocks must use the same ordering and weights as their forward operators. A zero-frequency projection is real; zero damping recovers the conventional Fourier transform. Neither special case removes dependence on the recorded bandwidth and background assumptions.[12,13,17]

The transform can be applied to conventionally acquired, band-limited post-stack seismic data and does not formally require broadband acquisition. Its usefulness nevertheless depends on the lowest reliable recorded frequencies, phase and amplitude calibration, the wavelet, record length, and noise. Damping reweights the available samples and cannot recreate independent observations outside the usable bandwidth. For conventional data, usable frequencies and damping coefficients should therefore be selected from the measured spectrum and tested for stability; the successful frequency range of a synthetic example should not be assumed for every survey.

4. Multi-channel inversion with Laplace–Fourier domain regularization

Having defined the forward operator in the LFD, we constructed the objective functional specifically for the inversion scheme (**Equation 15**):

$$J(L) = \min_L \left\| Y' - G'L'D'L \right\|_2^2 \quad (15)$$

where $\| \|_2^2$ signifies the L2 norm. Furthermore, to regularize the inversion process and accelerate convergence, we introduced an initial model constraint as follows (**Equation 16**):

$$J(L) = \min_L \left\| \alpha Y' - G'L'D'L \right\|_2^2 + \beta \left\| L - L \right\|_{02}^2 \quad (16)$$

where β denotes the weighting parameter assigned to the initial model, while L_0 signifies the initial model expressed in its logarithmic form. To facilitate the simultaneous inversion of multiple seismic traces, vertical and horizontal differential operators were subsequently incorporated into the objective function (**Equation 17**):

$$J(L) = \min_L \left\| Y' - G'L'D'L \right\|_2^2$$
$$+ \beta \left\| L - L_0 \right\|_2^2 + \gamma \left(\left\| LD_x \right\|_1^1 + \left\| D_y L \right\|_1^1 \right) \quad (17)$$

where γ weights the difference penalty, and $\| \|_1^1$ denotes the entrywise L1 norm. The horizontal and vertical difference operators are $D_x \in \boldsymbol{R}^{q \times (q-1)}$ and $D_y \in \boldsymbol{R}^{(n-1) \times n}$, acting as right and left multiplications, respectively.

Both operators use forward differences between adjacent samples only: LD_x subtracts neighboring traces and $D_y L$ subtracts neighboring time samples. There is no periodic wraparound or difference against an exterior zero-valued model; end-point pairs outside the model were omitted. Accordingly, the split variables and scaled dual arrays satisfy $d_x, C_x \in \boldsymbol{R}^{n \times (q-1)}$ and $d_y, C_y \in \boldsymbol{R}^{(n-1) \times q}$. Matrix L2 terms denote Frobenius norms, and L_1 terms sum absolute entries. For a complex residual, the corresponding squared

norm uses the Hermitian inner product; stacking its real and imaginary parts preserves that norm. The model difference uses the same adjacent-difference convention; padding only embeds the resulting reflectivity on the data grid and does not add boundary reflections.

To solve **Equation 17**, we first reformulated the objective function into a constrained optimization problem by introducing Lagrange multipliers. By substituting d_x and d_y with auxiliary variables LD_x and D_yL, we obtained **Equation 18**:

$$J(L) = \min_L \|Y' - G'L'D'L\|_2^2 + \beta\|L - L_0\|_2^2 + \gamma\left(\|d_x\|_1^1 + \|d_y\|_1^1\right)$$
$$s\,t\; d_x = LD_x \;\; d_y = D_yL \tag{18}$$

Next, the optimization task was converted into an unconstrained framework through the inclusion of dual terms in the objective function (**Equation 19**):

$$J(L) = \min_L \|Y' - G'L'D'L\|_2^2 + \beta\|L - L_0\|_2^2 + \gamma\left(\|d_x\|_1^1 + \|d_y\|_1^1\right)$$
$$+\lambda\left(\|d_x - LD_x + C_x\|_2^2 + \|d_y - D_yL + C_y\|_2^2\right) \tag{19}$$

where λ denotes the weighting coefficient (or penalty parameter) associated with the dual term, controlling the consistency between the Lagrange multipliers and the difference operators.

Leveraging the ADMM algorithm, the global objective function was decoupled into distinct sub-problems corresponding to the variables L, d_x, d_y, C_x, and C_y. To explain the procedure, we summarized the specific inversion workflow below. The proposed framework for multi-channel sparse inversion in the LFD is structured as follows in Algorithm 1.

Algorithm 1. Sparse multi-channel acoustic impedance inversion in the Laplace–Fourier domain using alternating direction method of multipliers

Input: Y, Y', W, D', G', L',L_0, β, γ, λ, Err, number of iteration = j;
Initial values: $k = 0$, $C_x^0 = C_y^0 = d_y^0 = d_x^0 = 0$, $L^0 = L_0$.

1. While $\frac{\|L^{j+1} - L^j\|_2^2}{\|L^j\|_2^2} > Err, do$

2. Update L^{j+1} by **Equations A6–A10**.

3. Update d_x^{j+1}, d_y^{j+1} by **Equations A11** and **A12**.

4. Update C_x^{j+1}, C_y^{j+1} by **Equations A14** and **A15**.

5. $j = j + 1$

6. End

Note: Model, auxiliary, and dual-variable updates are given in the Appendix.

5. Synthetic examples

5.1. Sensitivity of low-frequency acoustic impedance estimation to damping coefficients and frequency range

Two controlled experiments were conducted to investigate the effects of Laplace damping and frequency selection on low-frequency AI estimation. In the damping experiment, the frequency range was fixed at 0–4.008 Hz while the damping coefficients were varied. In the frequency experiment, the damping coefficients were fixed at [0, 2.5, 5]s^{-1} while the upper frequency limit was progressively increased. The initial model, wavelet, regularization parameters, and all other inversion settings were kept unchanged across the tests. The initial model was constructed by interpolating between the minimum and maximum values of the true AI. These experiments therefore constitute an idealized sensitivity benchmark.

Figure 4 compares the AI estimates obtained using different damping sets. All cases recover the broad low-frequency AI trend, although differences occur in the amplitudes and shapes of local variations. As the damping magnitude increases, low-frequency recovery initially improves and subsequently deteriorates, consistent with the preceding theoretical analysis. Among the tested damping sets, (σ =[0, 2.5, 5]) provides the best overall performance. These observations demonstrate that damping influences the estimated low-frequency trend, but larger damping coefficients do not necessarily yield better results.

Figure 5 illustrates the effect of expanding the frequency range. For the narrowest range, 0–2.004 Hz, the inverted AI is dominated by broad variations and does not reproduce many of the local variations in the true AI. As the upper frequency limit increases, the estimates resolve progressively more local structure and follow the major AI transitions more closely. Estimates obtained over wider frequency ranges also depart more clearly from the smooth initial model, indicating that the additional frequency samples influence the estimated AI structure.

These experiments demonstrate that AI estimation depends on both the Laplace damping coefficients and the selected frequency range. Damping modifies the estimated trend, but its effect is not simply monotonic. Expanding the frequency range improves the representation of local AI variations by introducing additional spectral constraints. Under the adopted assumptions regarding initialization, regularization, and amplitude calibration, the results support interpreting the recovered AI as a data-constrained, prior-dependent estimate rather than a unique recovery of missing low-frequency information.

To validate the feasibility and noise resilience of the

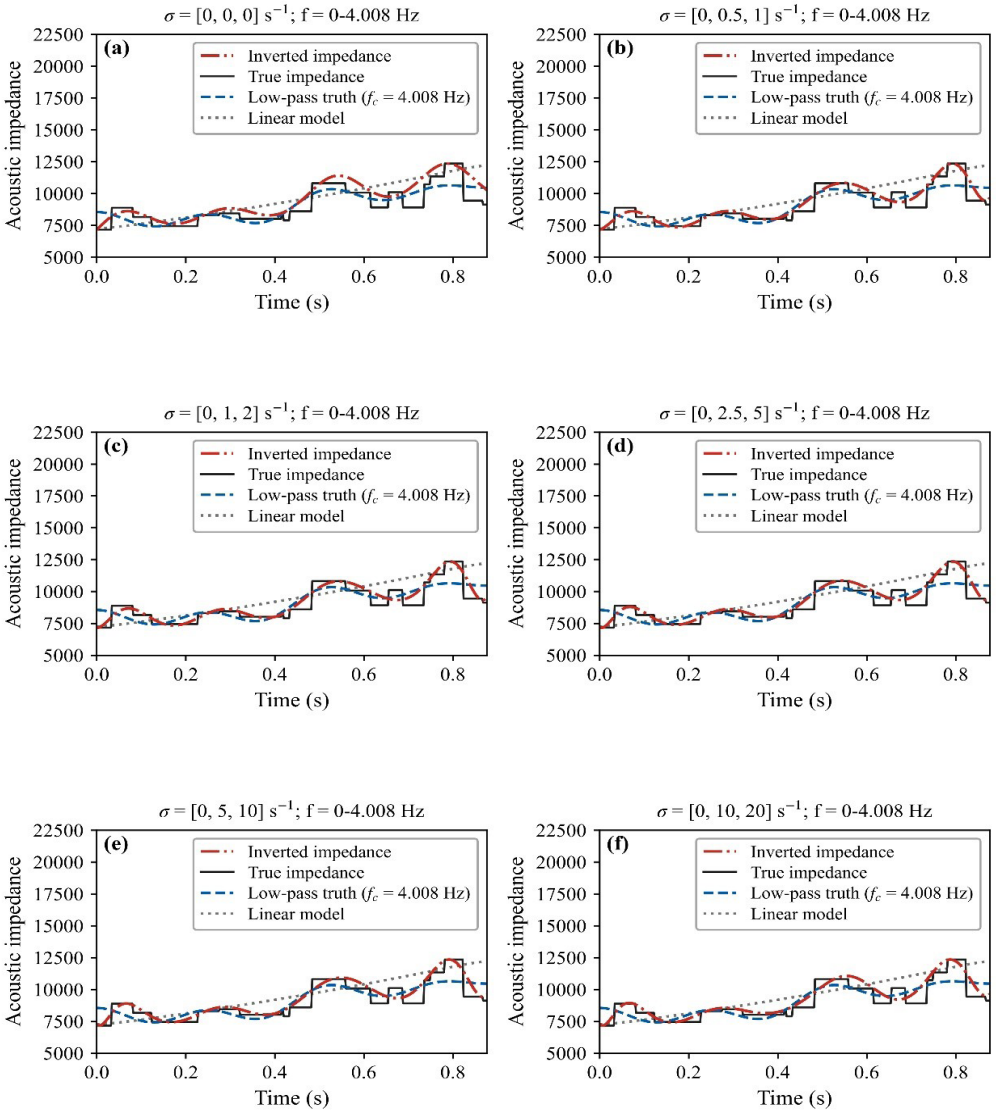


Figure 4. Acoustic impedance estimates at 0–4.008 Hz using damping sets (a) [0, 0, 0], (b) [0, 0.5, 1], (c) [0, 1, 2], (d) [0, 2.5, 5], (e) [0, 5, 10], and (f) [0, 10, 20] s^{-1}. Black, red, blue, and gray curves show the true, inverted, low-pass-reference, and initial impedances, respectively. The damping sets are denoted by σ. The blue reference is the true impedance low-pass filtered at 4.008 Hz and is not an input observation; time is in seconds.

proposed LFD sparse multi-channel inversion method, we utilized the Marmousi2 model to generate synthetic seismic traces. Single-channel data were extracted for testing under both noise-free and noisy conditions. Specifically, Figure 6 displays the synthetic records contaminated with 5%, 10%, and 20% Gaussian white noise, where the black curves denote the clean signals and the red curves depict the noisy data.

5.2. One-dimensional model testing

Figures 7 and 8 illustrate the single-channel AI inversion performance using a linear model and an LFD-derived low-frequency model as initial constraints, respectively. To establish a baseline, the linear model was constructed as a simplified macroscopic background, characterized by a continuous, linearly increasing AI trend with depth (or time). This linear gradient solely reflects the general compaction effect of subsurface strata and intrinsically lacks any specific structural variations or accurate low-frequency information. In these plots, the black, green, blue, and red lines denote the true AI, the linear model, the LFD low-frequency component, and the final inversion results,

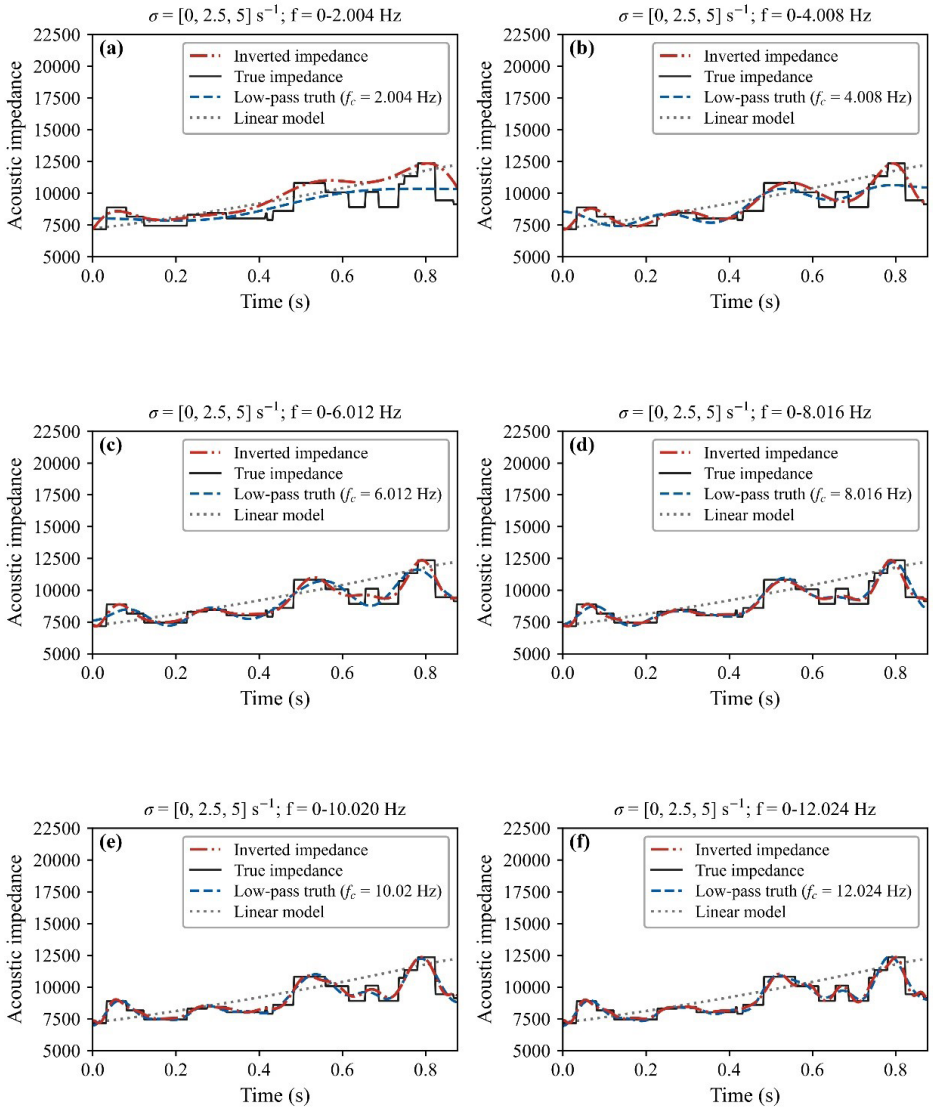


Figure 5. Acoustic impedance estimates using damping coefficients [0, 2.5, 5] s^{-1} and frequency ranges (a) 0–2.004, (b) 0–4.008, (c) 0–6.012, (d) 0–8.016, (e) 0–10.020, and (f) 0–12.024 Hz. Black, red, blue, and gray curves show the true, inverted, low-pass-reference, and initial impedances, respectively. The damping set is denoted by σ. Each blue reference uses the corresponding upper-frequency limit as its low-pass cutoff; time is in seconds.

respectively. Specifically, Figure 7 employs this linearly increasing background for initialization, whereas Figure 8 utilizes the LFD-extracted low-frequency information.

In noise-free scenarios, both methods successfully reconstructed the true AI. However, as highlighted by the dashed circles in Figures 7 and 8, significant disparities emerged with escalating noise levels. Lacking the accurate low-frequency constraints provided by the LFD, the inversion relying solely on the linear model struggled to converge, often becoming trapped in local minima within complex or transitional boundary regions. Conversely, by leveraging the LFD-extracted low-frequency information as the initial model, the predicted AI maintained high consistency with theoretical values, thereby validating the feasibility and robustness of the proposed approach.

5.3. Two-dimensional model testing under noise-free conditions

To comprehensively validate the effectiveness of the proposed method under complex subsurface conditions,

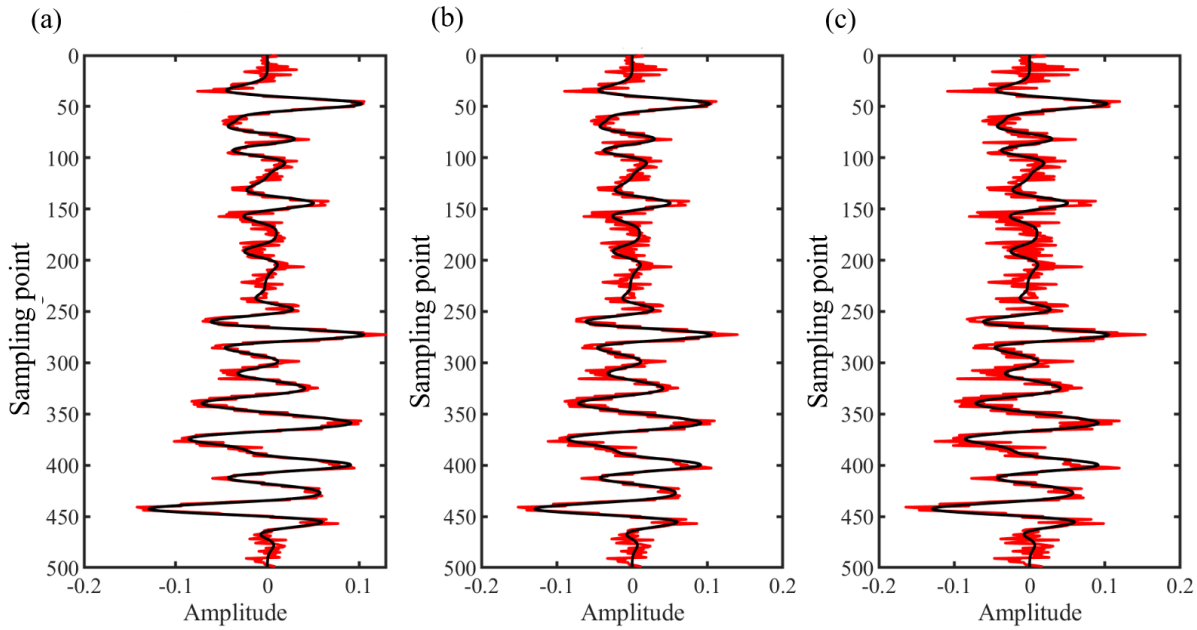


Figure 6. Synthetic seismic traces with (a) 5%, (b) 10%, and (c) 20% Gaussian white noise. Black and red curves denote clean and noisy data, respectively. Amplitude is plotted horizontally and sampling-point index vertically. The clean reference is identical in all three panels.

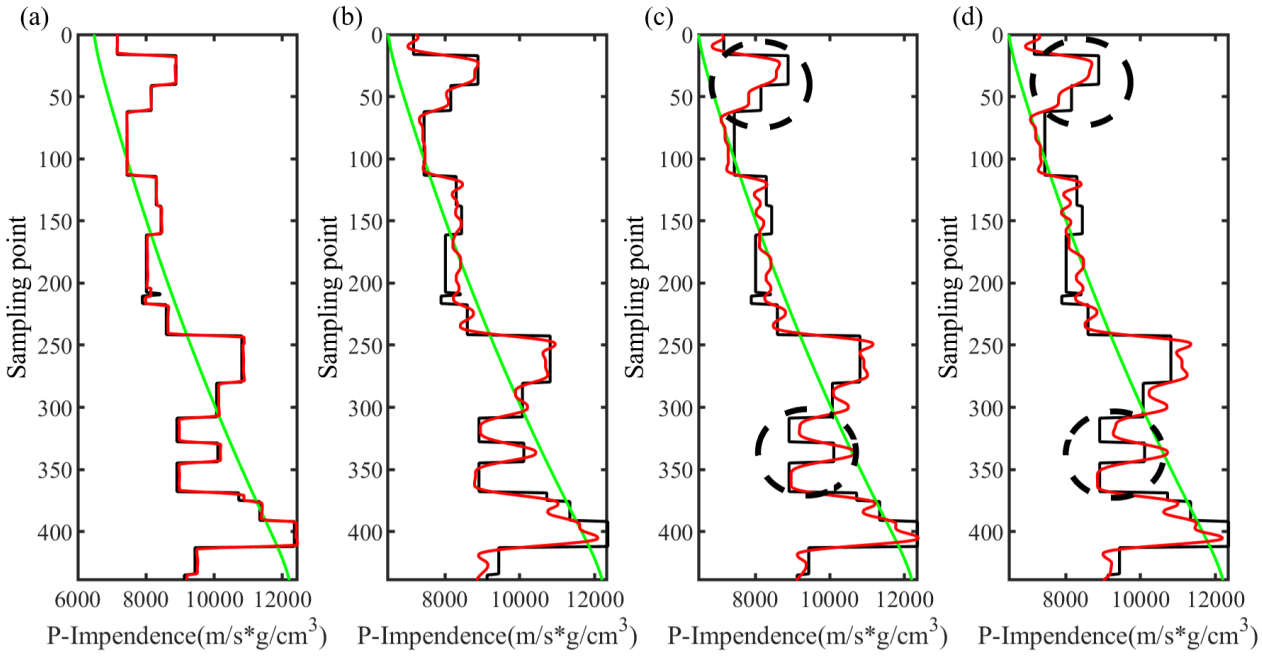


Figure 7. Single-channel acoustic impedance inversion with the linear background: (a) Noise-free; (b) 5%; (c) 10%; (d) 20% noise. Black, green, and red curves denote the true, initial, and inverted impedances, respectively. The sampling point index is plotted vertically and impedance horizontally. Dashed circles identify local discrepancies near stratigraphic transitions.

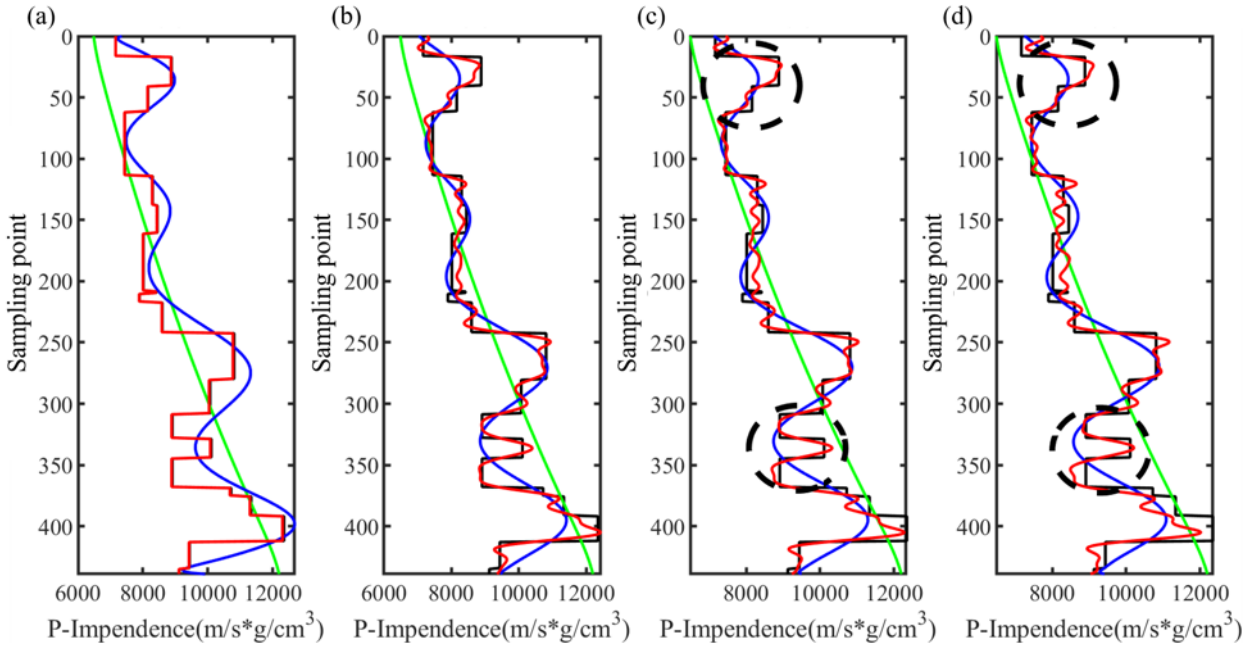


Figure 8. Single-channel acoustic impedance inversion with the Laplace–Fourier domain (LFD) background: (a) Noise-free; (b) 5%; (c) 10%; (d) 20% noise. Black, green, blue, and red curves denote the true, linear-background, LFD-background, and inverted impedances, respectively. The sampling point index is plotted vertically and impedance horizontally. Dashed circles mark the intervals compared with the linear-background inversion.

a representative section of the 2D Marmousi2 model was selected for testing. As depicted in Figure 9a, this section comprises 800 traces with 439 sampling points per trace. The model features highly complex structural architectures, characterized by distinct stratigraphic pinch-outs and dramatic lateral variations, which pose severe challenges to the boundary-delineation capabilities of inversion algorithms.

For an idealized test of low-frequency estimation without a detailed stratigraphic background, we constructed a simplified linear initial model (Figure 9b). Consistent with the one-dimensional tests, this baseline model was generated solely via linear interpolation between the minimum and maximum AI values across the depth profile. It represents merely a continuous, linearly increasing background gradient driven by generic compaction, completely devoid of any localized geological structural information.

The background range is inherited from the reference AI model. Consequently, this synthetic example assesses estimation of structure within an assumed absolute scale, not identification of that scale from reflection data alone.

Building upon this baseline, we systematically compared four distinct inversion strategies to decouple the contributions of the algorithmic components: (i) linear-single: single-channel inversion relying solely on the linear background model; (ii) LFD-single: single-channel inversion initialized with LFD-extracted low-frequency constraints; (iii) linear-multi: multi-channel inversion utilizing the linear background model; and (iv) LFD-multi: the proposed multi-channel simultaneous inversion integrated with LFD low-frequency constraints.

Figure 10 illustrates the low-frequency AI background successfully reconstructed directly from the band-limited seismic data using the proposed LFD mechanism. In stark contrast to the featureless linear initial model, this LFD-derived result accurately recovers the large-scale AI trends and structural outlines of the strata, thereby demonstrating the superiority of the LFD in decoupling and retrieving missing low-frequency components.

Figure 11 displays the comparison of inversion results for the four methods under noise-free conditions. The linear-single method (Figure 11a), due to a severe lack of low-frequency information, can only recover relative changes in AI, leading to substantial absolute value deviations (as highlighted by the black rectangle) and an inability to identify pinch-out points. In contrast, the LFD-single method (Figure 11b) benefits from the low-frequency constraints provided by the LFD and accurately recovers the background AI; however, it exhibits obvious

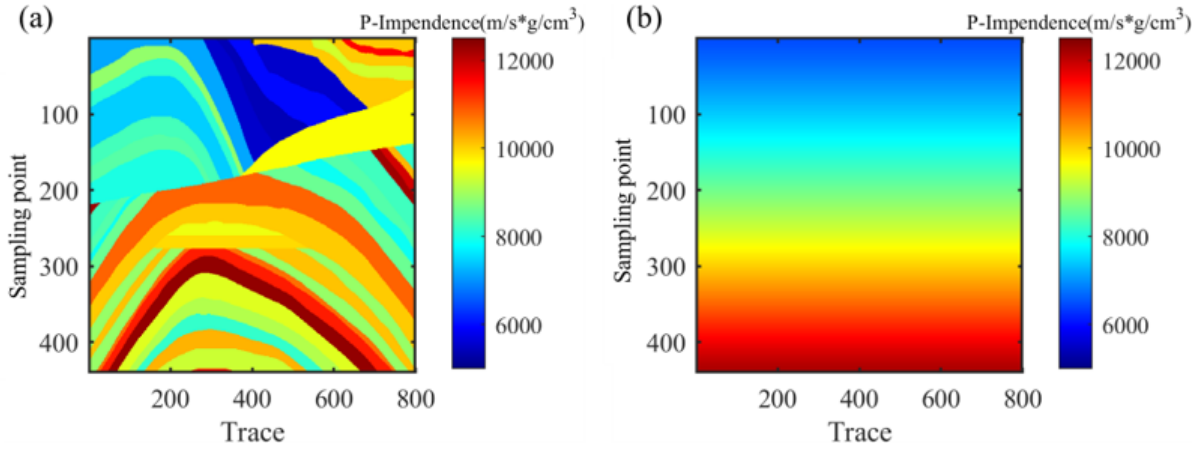


Figure 9. Two-dimensional Marmousi2 acoustic impedance models: (a) true model; (b) linear initial model. Each model contains 800 traces and 439 samples per trace. The axes are trace number and sampling-point index; colors represent acoustic impedance. The initial model contains no detailed stratigraphic structure.

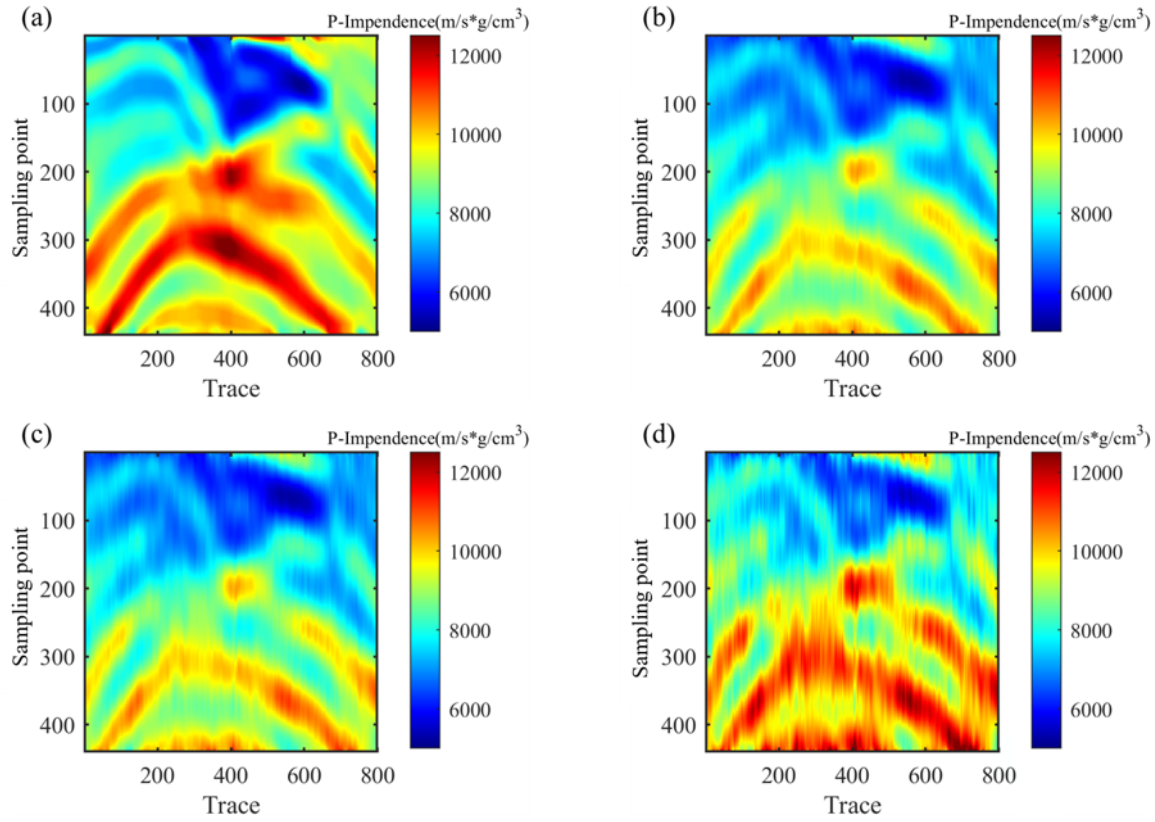


Figure 10. Two-dimensional low-frequency acoustic impedance estimates: (a) Noise-free; (b) 5%; (c) 10%; (d) 20% noise. The axes are trace number and sampling-point index; colors represent estimated acoustic impedance. Panels compare background structure and lateral artifacts as noise increases.

lateral discontinuities (vertical striping effects), which is an inherent defect of trace-by-trace calculations that lack spatial constraints. The linear-multi method (Figure 11c) improves lateral continuity through spatial regularization, but due to the inaccurate low-frequency background, it still suffers from severe layer positioning errors at pinch-

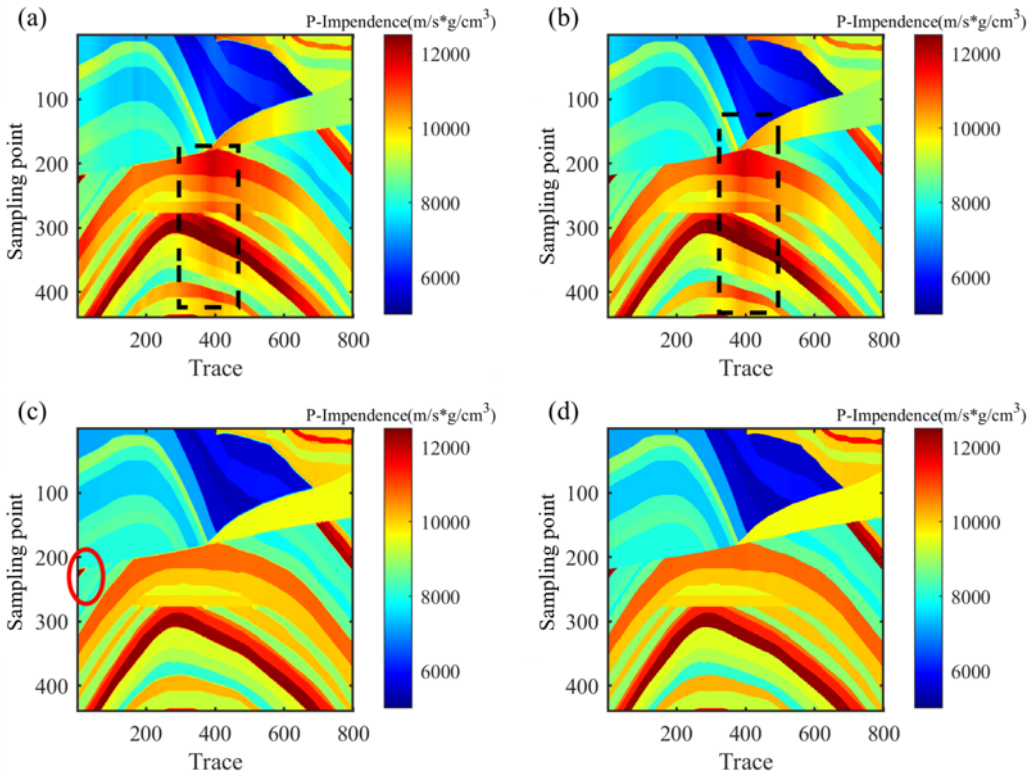


Figure 11. Noise-free two-dimensional acoustic impedance inversion: (a) linear-single; (b) LFD-single; (c) linear-multi; (d) LFD-multi. LFD-multi implementation parameters: $\beta = 6.479 \times 10^{-9}$, $\gamma = 1.257 \times 10^{-8}$, $\lambda = 2.126 \times 10^{-4}$. Colors represent acoustic impedance. Linear and LFD denote the linear and estimated low-frequency backgrounds; single and multi denote independent-trace and joint multi-trace inversion, respectively.
Abbreviation: LFD: Laplace–Fourier domain.

out points and complex structural areas (marked by the red circle). The proposed LFD-multi method (Figure 11d) combines both advantages: the LFD strategy ensures the accuracy of low-frequency components, while the multi-channel sparse regularization utilizes the spatial correlation of adjacent traces to eliminate lateral jitter, clearly delineating pinch-out terminations and stratigraphic boundaries.

To quantitatively evaluate inversion accuracy, Figure 12 presents the absolute error distribution maps. The linear model-based methods (Figure 12a and 12c) exhibit high background errors across the entire profile, indicating that the absence of low frequencies is the primary source of error. Although the LFD-single method (Figure 12b) reduces background error, it presents high-frequency vertical striping errors. The LFD-multi method (Figure 12d) achieves the smallest and most uniformly distributed residual errors, further confirming that the proposed method can achieve high-precision, high-resolution AI inversion under the adopted background-scale assumptions by combining low-frequency estimation with spatial constraints.

Figure 13 presents the signal-to-noise ratio (SNR) distribution curves, further quantifying the reconstruction accuracy of the four inversion strategies under ideal (noise-free) conditions. The quantitative evaluation results demonstrate that the Laplace frequency domain multi-channel inversion achieves the highest SNR gains across every seismic trace, primarily due to its optimized operator structure and multi-channel constraint mechanism. Compared to traditional approaches, the Laplace frequency domain multi-channel inversion exhibits superior convergence and noise resilience. By effectively integrating lateral constraint information into the objective function, this method ensures significantly better spatial continuity and stability in the inversion results, effectively suppressing numerical instabilities caused by random errors. This ability to maintain high resolution while ensuring robust performance provides a solid theoretical foundation for the application of this method to practical, complex geological tasks and low-SNR data.

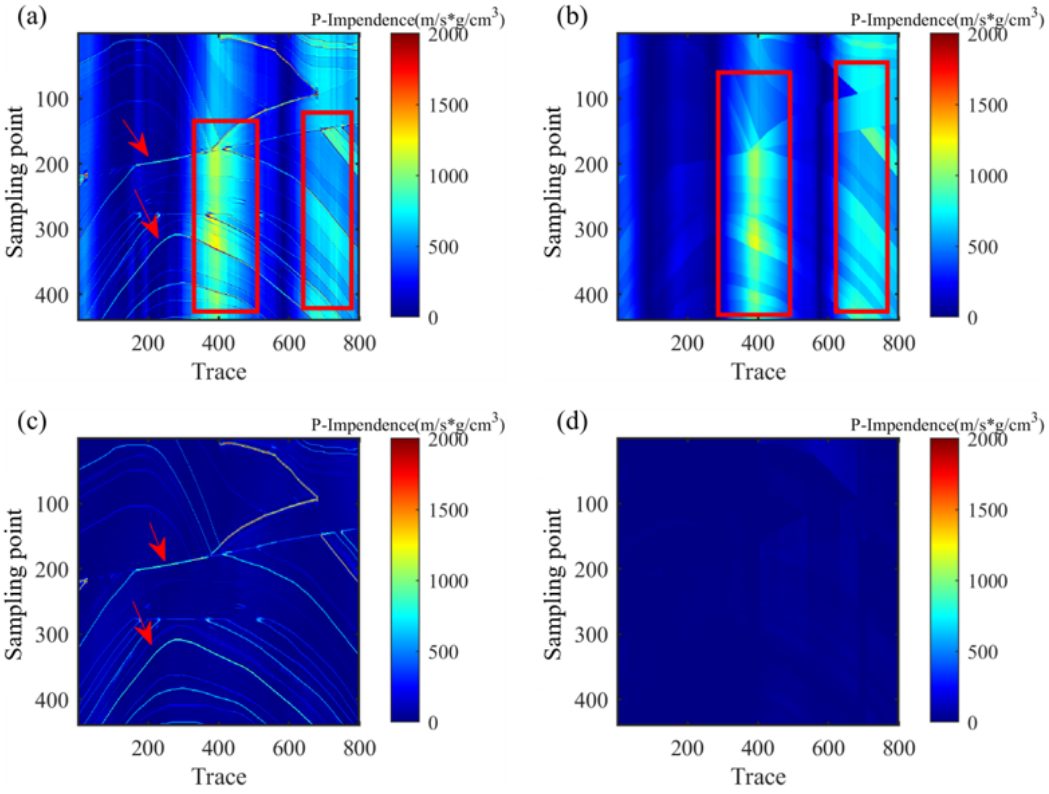


Figure 12. Absolute acoustic impedance errors for the noise-free two-dimensional test: (a) linear-single; (b) LFD-single; (c) linear-multi; (d) LFD-multi. Colors show the absolute difference from the true model on a common scale. Red boxes and arrows highlight localized and interface-related errors.
Abbreviation: LFD: Laplace–Fourier domain.

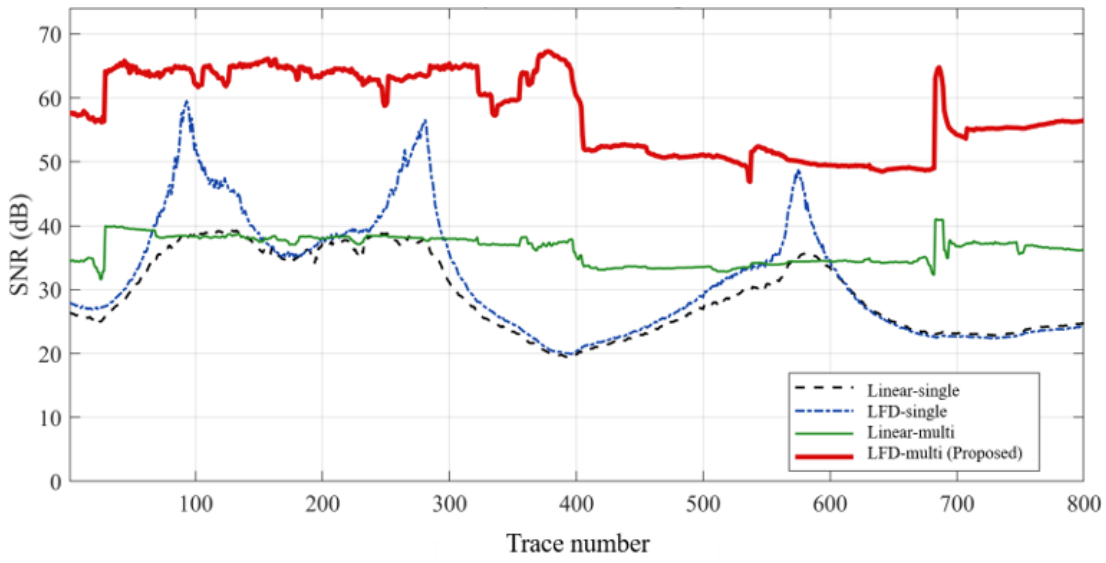


Figure 13. Trace-by-trace reconstruction SNR for the noise-free two-dimensional test. Curves denote linear-single, LFD-single, linear-multi, and LFD-multi, as indicated in the legend. The axes are trace number and SNR in decibels. Higher SNR indicates smaller acoustic impedance reconstruction error relative to the true model.
Abbreviations: LFD: Laplace–Fourier domain; SNR: Signal-to-noise ratio.

5.4. Two-dimensional model testing under noise conditions

To validate the robustness of the proposed inversion strategy in noisy environments, synthetic seismic records were contaminated with 5%, 10%, and 20% Gaussian white noise, respectively. The inversion results, absolute error distributions, and trace-by-trace SNR evaluations are presented in Figures 14–22. Specifically, Figures 14–16 correspond to the 5% noise level, Figures 17–19 to 10%, and Figures 20–22 to 20%.

As the noise level intensifies, the performance divergence among the four strategies becomes pronounced. In the AI profiles (Figures 14, 17, and 20), the regions enclosed by black dashed boxes (specifically in Figures 14a,b, 17a,b, and 20a,b) exhibit severe instability. These marked areas indicate that single-channel methods are highly sensitive to noise, resulting in high-frequency oscillations and significant deviation from true AI values. Specifically, the lack of lateral constraints in single-channel approaches causes neighboring traces to vary independently, disrupting the lateral continuity of sedimentary events. Such artifacts can lead to false interpretations of stratigraphic heterogeneity, making it difficult to distinguish between actual geological thin beds and noise-induced anomalies. In contrast, the multi-channel methods demonstrate superior robustness. By leveraging lateral spatial correlations, random noise is effectively suppressed, maintaining stratigraphic integrity even under 20% noise conditions.

The absolute error maps (Figures 15, 18, and 21) further elucidate the impact of low-frequency and spatial constraints. Red solid circles identify areas of significant error accumulation, while red arrows point to sharp lithological interfaces and pinch-out points where traditional methods typically fail. A comparative analysis reveals that large systematic discrepancies (indicated by the red circles) are persistent in the linear and single-channel models (Figures 15a–c, 18a–c, and 21a–c). It is worth noting that the errors in the linear models (Figures 15c, 18c, and 21c) manifest primarily as a low-frequency bias—a direct consequence of the band-limited nature of the input data that prevents the recovery of the absolute impedance baseline. Meanwhile, the single-channel LFD method (Figures 15b, 18b, and 21b), while recovering the background trend, suffers from high-amplitude random errors due to its inability to distinguish between signal and noise. In contrast, the proposed LFD multi-channel inversion (Figures 15d, 18d, and 21d) demonstrates superior accuracy with a uniform and low-magnitude error distribution. The absence of high-error indicators in Figures 15d, 18d, and 21d visually confirms that the proposed method effectively recovers true subsurface physical properties and preserves sharp geological boundaries even in high-noise environments.

To further quantify the noise resilience of the algorithms, Figures 16, 19, and 22 present the trace-by-trace SNR evaluation results for the four inversion methods. The quantitative SNR evaluations corroborate the qualitative analysis discussed above. While the reconstruction accuracy of all methods naturally decreases as noise levels increase, the Laplace frequency domain multi-channel inversion consistently maintains the highest SNR values across all noise intensities, demonstrating the strongest robustness. The linear multi-channel inversion performs second best, benefiting from the inherent advantages of multi-channel constraints in suppressing random noise. However, its SNR is fundamentally capped by the background model error. The significant SNR gap between the proposed method and the linear multi-channel method highlights that simply suppressing noise is insufficient; accurate low-frequency recovery is equally vital for high-fidelity inversion.

The noise robustness of LFD-multi was evaluated quantitatively through 2D AI inversion tests at different noise power ratios. As summarized in Table 1, without noise, the inversion achieved a root-mean-square error of 608.174, a Pearson correlation coefficient of 0.9302, and a relative error of 6.601%. As the noise power ratio increased from 5% to 20%, the root-mean-square error increased from 825.806 to 887.040, the relative error increased from 8.964% to 9.628%, and the correlation coefficient decreased from 0.8702 to 0.8492. Although noise reduced inversion accuracy, the errors increased relatively gradually across the tested noisy conditions. Even at a noise power ratio of 20%, the correlation coefficient remained at 0.8492, and the relative error was 9.628%, indicating that the inverted model retained good overall agreement with the true model. The relatively small variability of the reported metrics also suggests consistent performance across noise realizations. Overall, the proposed method demonstrates resistance to noise in this 2D synthetic test, although its accuracy remains dependent on the noise level.

To provide a more intuitive comparison of inversion details, Figures 23 and 24 display the single-channel extraction results of the linear multi-channel inversion and the Laplace frequency domain multi-channel inversion against the true model under varying noise levels. As observed in Figure 23 (linear multi-channel inversion), the method accurately identifies the positions of reflection interfaces under noise-free conditions. However, as the noise intensity increases from 5% to 20%, significant spurious oscillations appear in the inversion profiles. The fidelity of waveform reconstruction gradually diminishes,

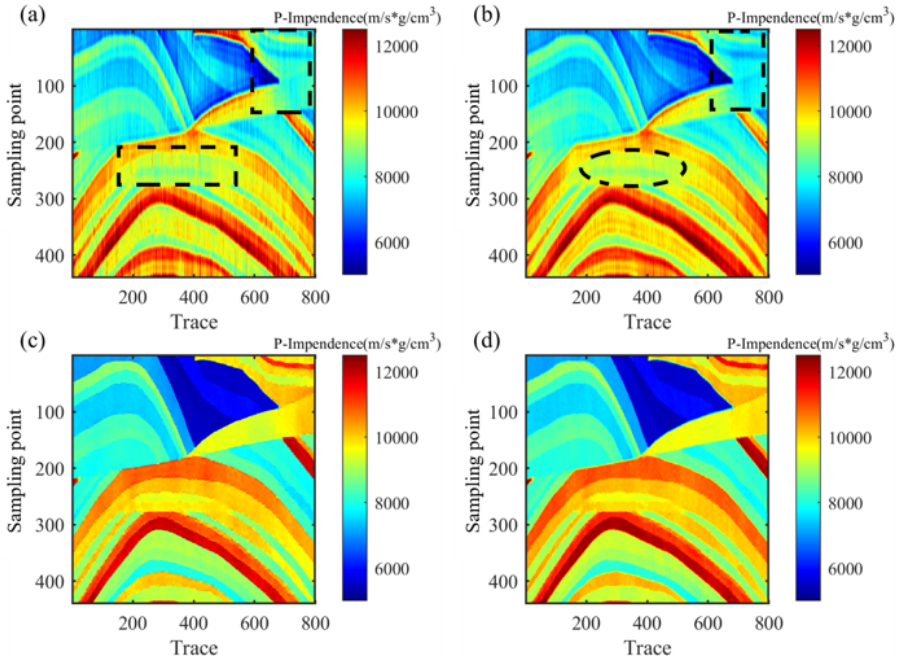


Figure 14. Two-dimensional acoustic impedance inversion with 5% Gaussian white noise: (a) linear-single; (b) LFD-single; (c) linear-multi; (d) LFD-multi. LFD-multi implementation parameters: $\beta = 1.265 \times 10^{-4}$, $\gamma = 1.581 \times 10^{-1}$, $\lambda = 3.557 \times 10^{-2}$. Colors represent acoustic impedance. Linear and LFD denote the linear and estimated low-frequency backgrounds; single and multi denote independent-trace and joint multi-trace inversion.
Abbreviation: LFD: Laplace–Fourier domain.

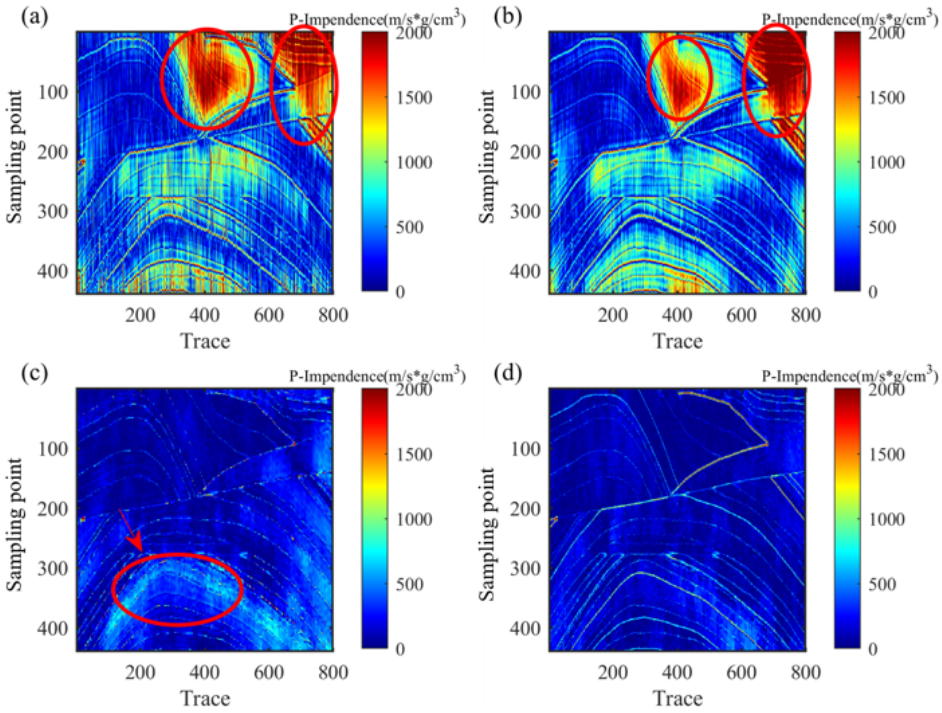


Figure 15. Absolute acoustic impedance errors with 5% Gaussian white noise: (a) linear-single; (b) LFD-single; (c) linear-multi; (d) LFD-multi. Colors show the absolute difference from the true model on a common scale. Red ellipses and arrows mark localized error concentrations and interfaces.
Abbreviation: LFD: Laplace–Fourier domain.

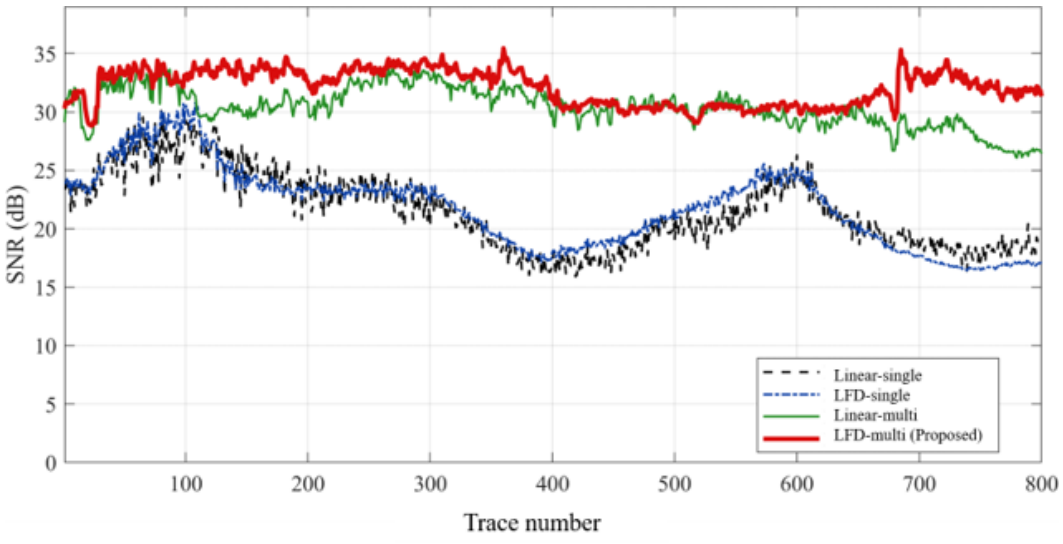


Figure 16. Trace-by-trace reconstruction SNR with 5% Gaussian white noise. Curves denote linear-single, LFD-single, linear-multi, and LFD-multi, as indicated in the legend. The axes are trace number and SNR in decibels. Higher SNR indicates smaller acoustic impedance reconstruction error relative to the true model.
Abbreviations: LFD: Laplace–Fourier domain; SNR: Signal-to-noise ratio.

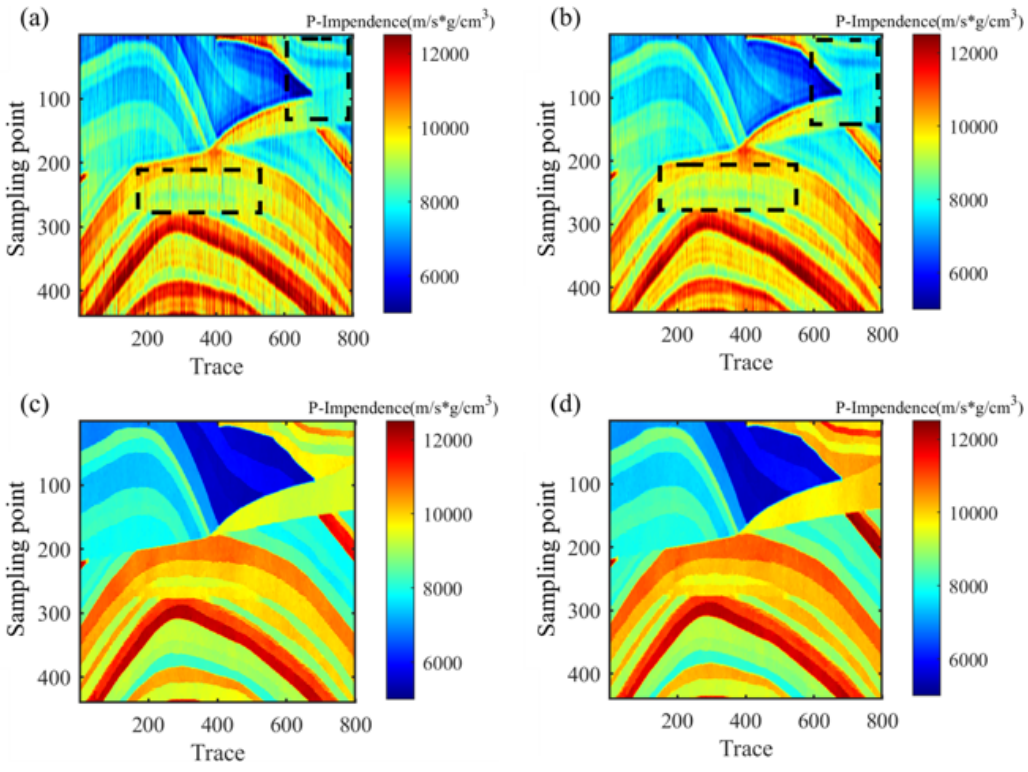


Figure 17. Two-dimensional acoustic impedance inversion with 10% Gaussian white noise: (a) linear-single; (b) LFD-single; (c) linear-multi; (d) LFD-multi. LFD-multi implementation parameters: $\beta = 2.750 \times 10^{-4}$, $\gamma = 9.000 \times 10^{-2}$, $\lambda = 3.000 \times 10^{-2}$. Colors represent acoustic impedance. Linear and LFD denote the linear and estimated low-frequency backgrounds; single and multi denote independent-trace and joint multi-trace inversion.
Abbreviation: LFD: Laplace–Fourier domain.

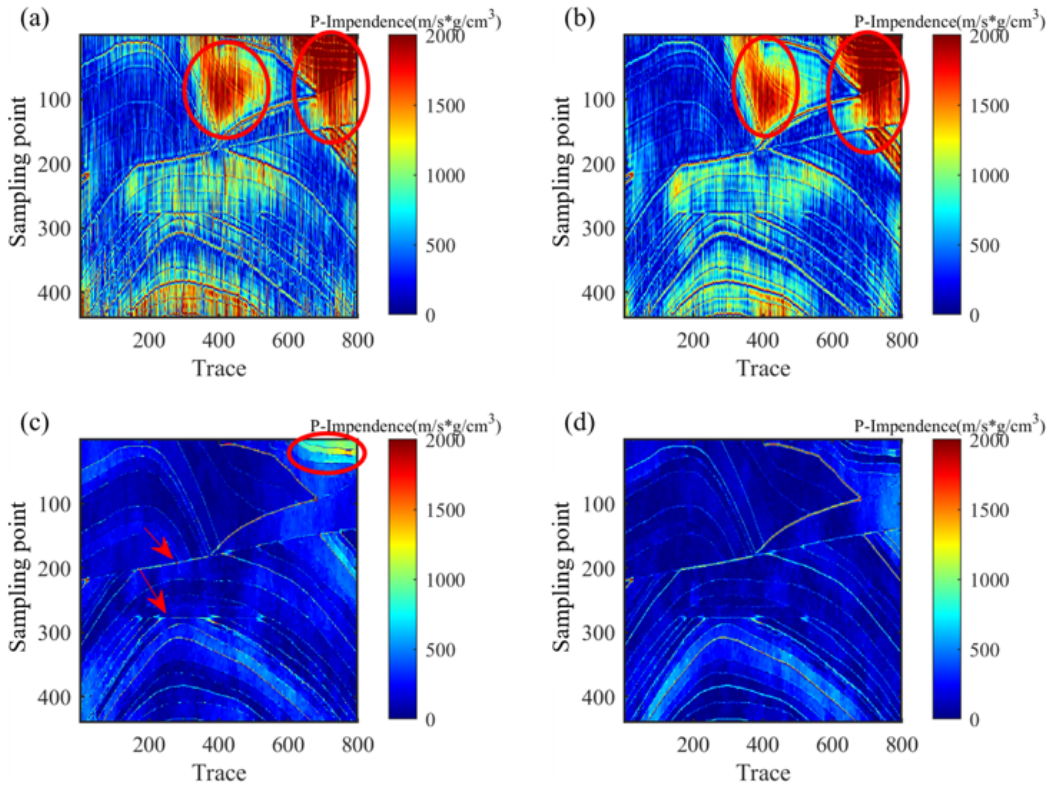


Figure 18. Absolute acoustic impedance errors with 10% Gaussian white noise: (a) linear-single; (b) LFD-single; (c) linear-multi; (d) LFD-multi. Colors show the absolute difference from the true model on a common scale. Red ellipses and arrows mark localized error concentrations and interfaces.
Abbreviation: LFD: Laplace–Fourier domain.

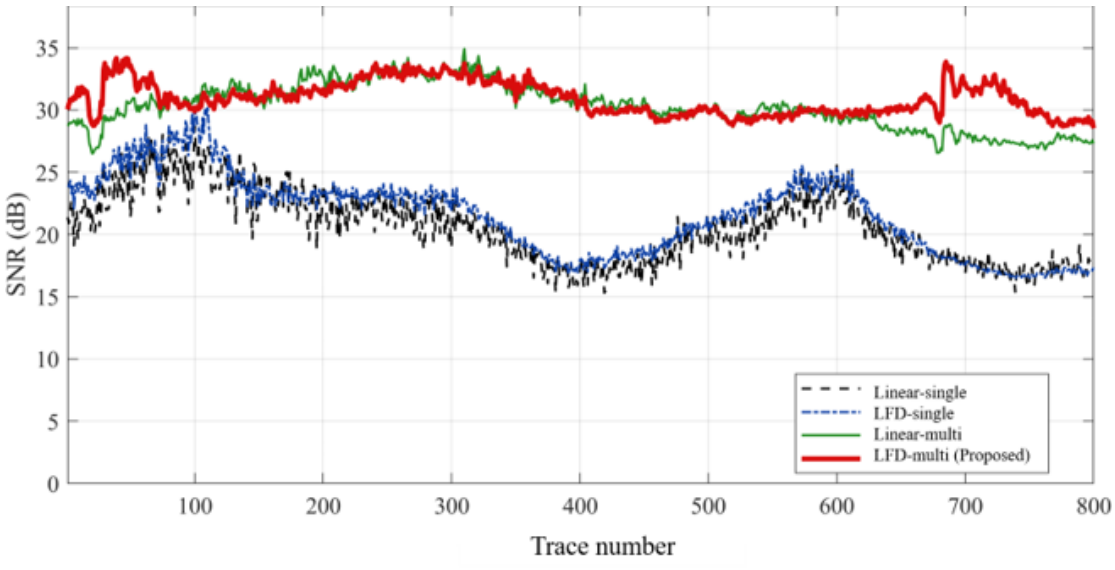


Figure 19. Trace-by-trace reconstruction SNR with 10% Gaussian white noise. Curves denote linear-single, LFD-single, linear-multi, and LFD-multi, as indicated in the legend. The axes are trace number and SNR in decibels. Higher SNR indicates smaller acoustic impedance reconstruction error relative to the true model.
Abbreviations: LFD: Laplace–Fourier domain; SNR: Signal-to-noise ratio.

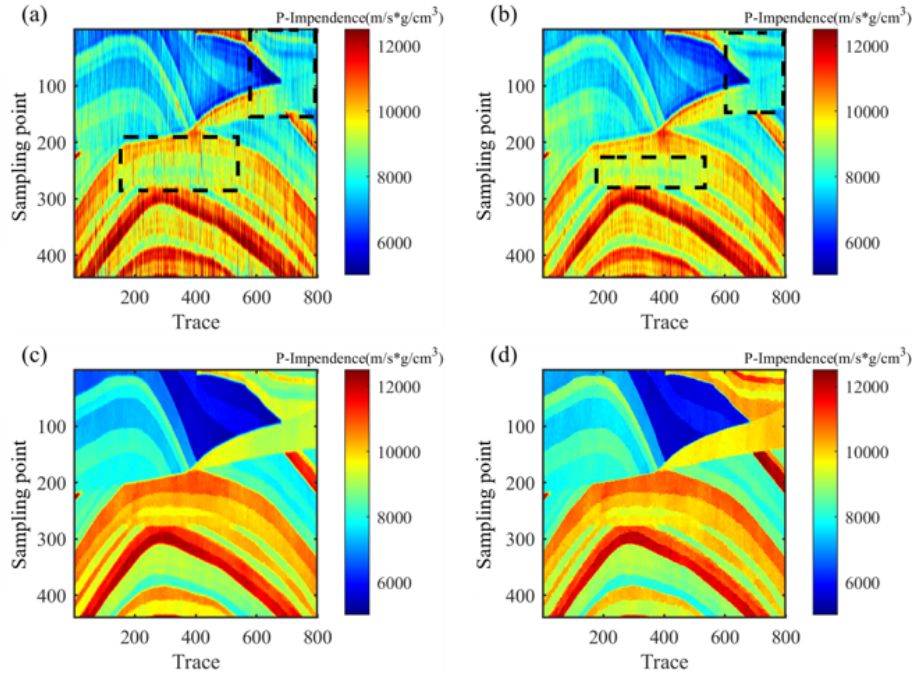


Figure 20. Two-dimensional acoustic impedance inversion with 20% Gaussian white noise: (a) linear-single; (b) LFD-single; (c) linear-multi; (d) LFD-multi. LFD-multi implementation parameters: $\beta = 2.000 \times 10^{-4}$, $\gamma = 3.162 \times 10^{-1}$, $\lambda = 1.000 \times 10^{-1}$. Colors represent acoustic impedance. Linear and LFD denote the linear and estimated low-frequency backgrounds; single and multi denote independent-trace and joint multi-trace inversion.
Abbreviation: LFD: Laplace–Fourier domain.

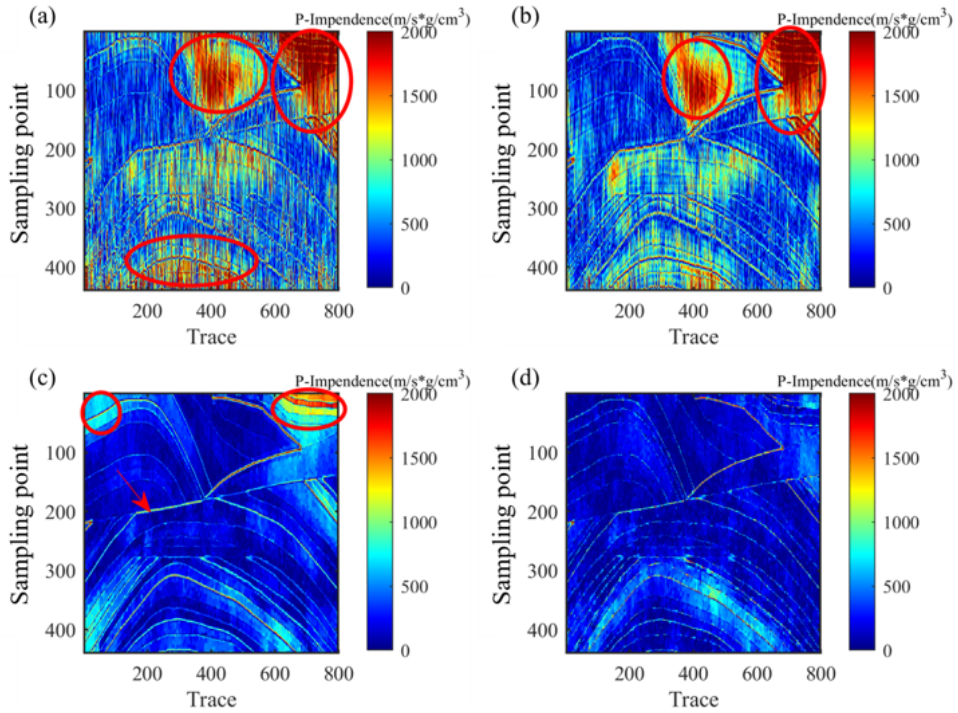


Figure 21. Absolute acoustic impedance errors with 20% Gaussian white noise: (a) linear-single; (b) LFD-single; (c) linear-multi; (d) LFD-multi. Colors show the absolute difference from the true model on a common scale. Red ellipses and arrows mark localized error concentrations and interfaces.
Abbreviation: LFD: Laplace–Fourier domain.

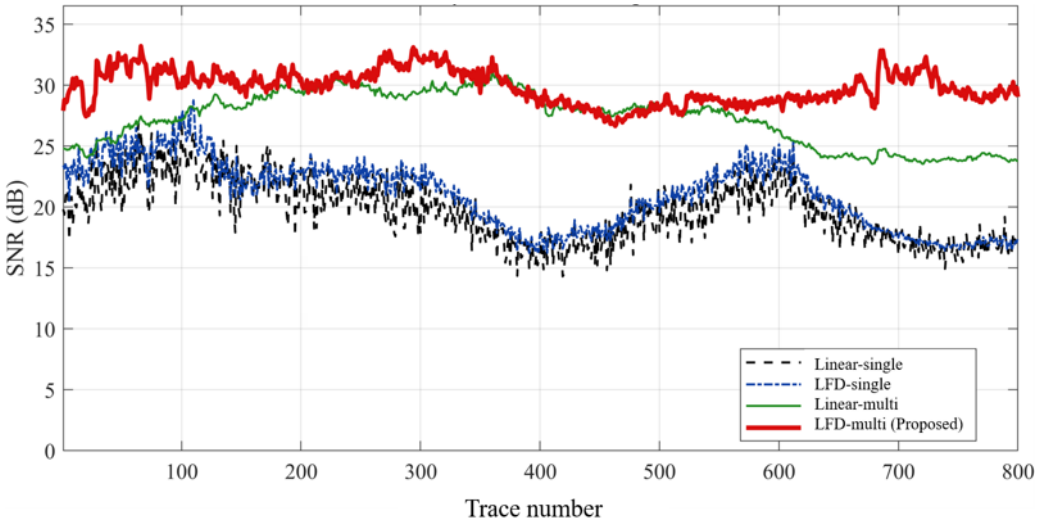


Figure 22. Trace-by-trace reconstruction SNR with 20% Gaussian white noise. Curves denote linear-single, LFD-single, linear-multi, and LFD-multi, as indicated in the legend. The axes are trace number and SNR in decibels. Higher SNR indicates smaller acoustic impedance reconstruction error relative to the true model.
Abbreviations: LFD: Laplace–Fourier domain; SNR: Signal-to-noise ratio.

with the inversion results exhibiting pronounced numerical instability, particularly in deep regions with weak reflections.

Table 1. Noise robustness of LFD-multi in two-dimensional acoustic impedance inversion

Noise power ratio (%)	RMSE	Correlation coefficient	Relative error (%)
0%	608.174	0.9302	6.601
5%	825.806 ± 32.101	0.8702 ± 0.0125	8.964 ± 0.348
10%	848.456 ± 34.708	0.8602 ± 0.0134	9.209 ± 0.377
20%	887.040 ± 45.183	0.8492 ± 0.0199	9.628 ± 0.490

Note: Noise levels are power ratios. RMSE, global Pearson correlation, and relative Frobenius error compare inverted and unfiltered true impedances. Noisy entries report mean ± sample standard deviation; the noise-free entry is a single result.
Abbreviations: LFD: Laplace–Fourier domain; RMSE: Root-mean-square error.

In contrast, the Laplace frequency-domain multi-channel inversion results shown in Figure 24 are significantly superior. Under noise-free conditions (Figure 24a), the inversion results agree closely with the true model, enabling precise characterization of thin-layer information. In the subsequent noisy tests (Figure 24b–d), the Laplace frequency-domain multi-channel inversion maintains robust tracking capabilities despite the progressive increase in environmental interference. Even at a high noise level of 20%, the main features of the AI profile remain identifiable, with minimal noise-induced distortion.

6. Field data example

We applied the inversion framework to a field seismic profile from an area characterized by thin-bedded sandstone reservoirs. Figure 25 compares six AI sections: linear-single, LFD-single, linear-multi, LFD-multi, time-domain Bayesian inversion, and LFD Bayesian inversion. The two Bayesian results provide additional comparisons for evaluating whether the proposed method combines coherent impedance structure with distinct local interfaces. Here, single denotes independent-trace inversion and multi denotes the joint inversion of neighboring traces; all six displayed sections represent AI.

The Bayesian comparators in Figure 25e and 25f are single-trace maximum a posteriori estimates of log AI. Both Bayesian objectives combine a working Gaussian data likelihood, an isotropic Gaussian prior centered on a background log-impedance model, and a Laplace prior on vertical log-impedance differences ($p = 1$). There is no lateral prior or trace-to-trace coupling.

In Figure 25a–d, the multi-channel results show more

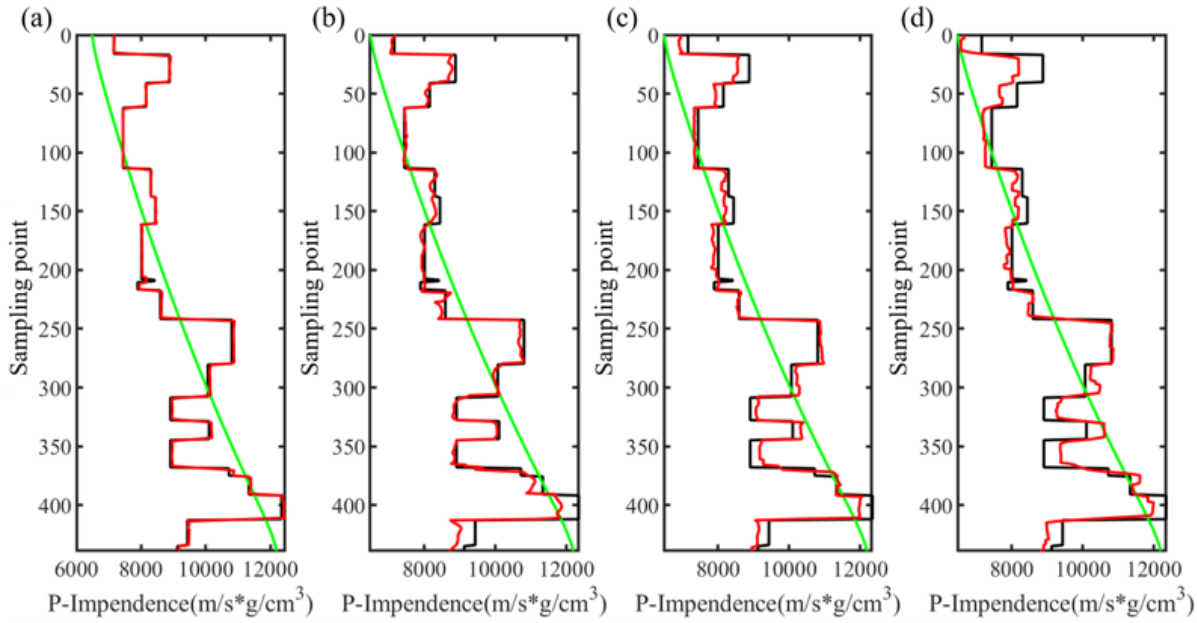


Figure 23. Acoustic impedance traces extracted from two-dimensional linear-multi inversion: (a) noise-free; (b) 5%; (c) 10%; (d) 20% noise. Black, green, and red curves denote the true, initial, and inverted impedances, respectively. These are trace extractions from joint multi-channel inversion, not independent single-channel results. The sampling point index is plotted vertically and acoustic impedance horizontally.

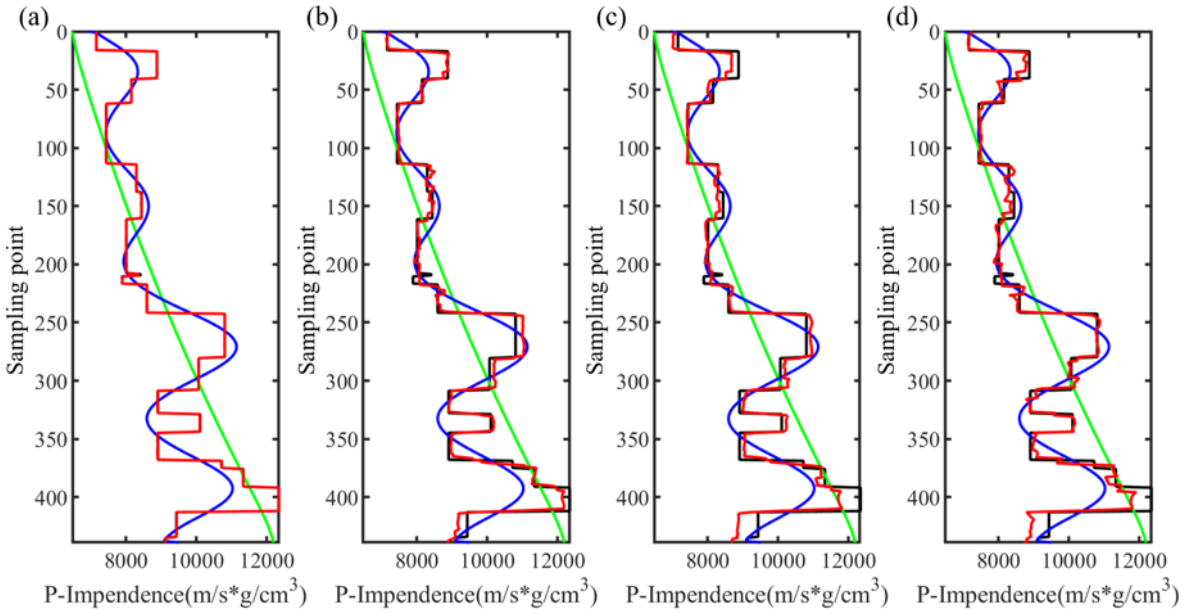


Figure 24. Acoustic impedance traces extracted from two-dimensional LFD-multi inversion: (a) noise-free; (b) 5%; (c) 10%; (d) 20% noise. Black, green, blue, and red curves denote the true, linear-background, LFD-background, and inverted impedances, respectively. These are trace extractions from joint multi-channel inversion. The sampling point index is plotted vertically and acoustic impedance horizontally; the blue curve is the low-frequency background.
Abbreviation: LFD: Laplace–Fourier domain.

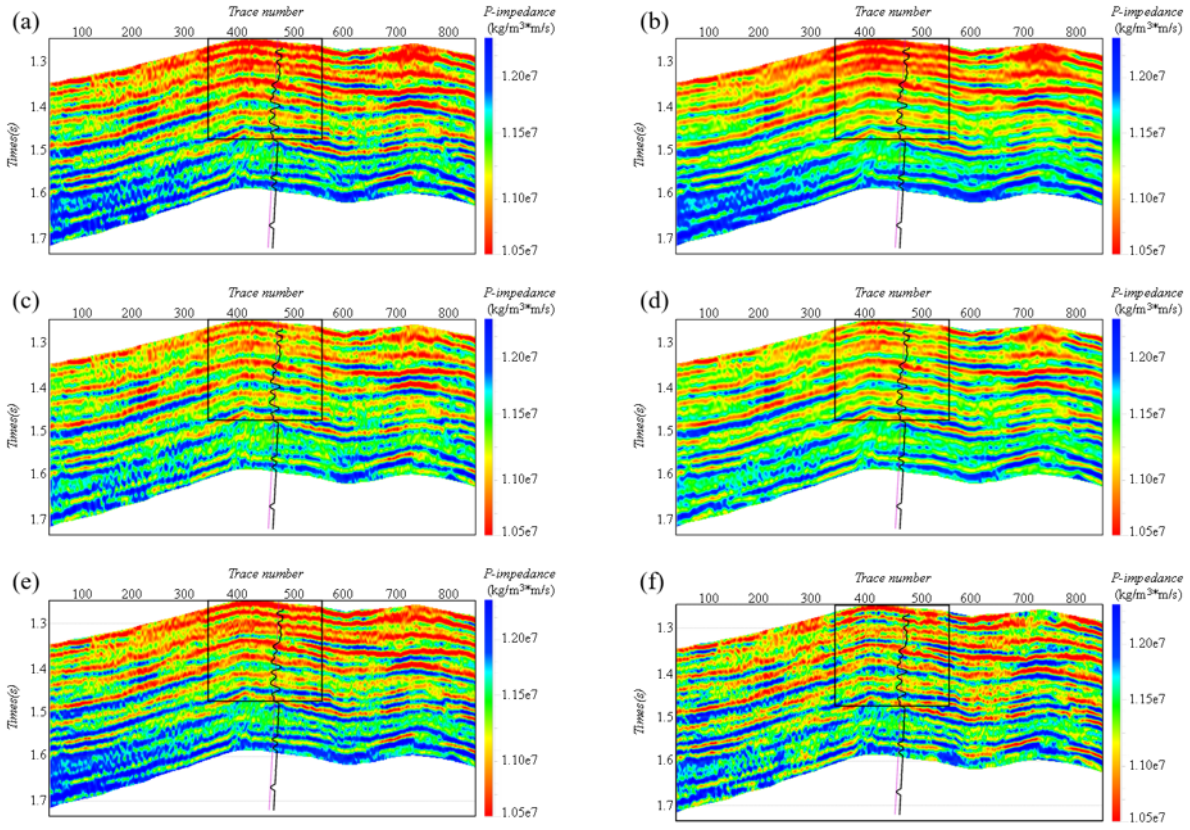


Figure 25. Field acoustic impedance inversion results: (a) linear-single; (b) LFD-single; (c) linear-multi; (d) LFD-multi; (e) time-domain Bayesian inversion; (f) LFD Bayesian inversion. Single and multi denote independent-trace and joint multi-trace inversion; linear and LFD identify the linear and estimated low-frequency backgrounds. Black rectangles mark the comparison interval, and overlaid well curves provide a local comparison. The horizontal and vertical axes denote trace number and time (s), respectively; acoustic impedance is in kg m^{-2} s^{-1}.
Abbreviation: LFD: Laplace–Fourier domain.

laterally continuous impedance bands and fewer trace-to-trace fluctuations than their single-channel counterparts. The highlighted interval illustrates the difference between continuity and local contrast. Linear-multi produces continuous boundaries, showing the contribution of lateral coupling even with a linear background. LFD-multi retains this continuity while giving a more distinct separation of neighboring high- and low-impedance bands. This combination is consistent with the use of an estimated low-frequency background together with sparse and lateral regularization. The comparison concerns the appearance of the inverted interfaces and does not by itself establish the true thickness of sub-tuning layers.

The time-domain Bayesian section in Figure 25e reproduces the main folded structure, but local impedance contrasts and the separation of neighboring bands are less consistently expressed than in LFD-multi. The LFD Bayesian section in Figure 25f also follows the regional structural trend and shows local contrast differences relative to the time-domain result. However, local trace-to-trace fluctuations remain visible, particularly in the deeper part of the displayed interval. Compared with these two Bayesian sections, LFD-multi in Figure 25d provides a clearer balance between lateral continuity and the preservation of narrow impedance contrasts. For this calibrated comparison, the observed advantage is consistent with combining LFD background estimation with joint multi-trace sparse regularization, rather than in the domain transformation alone.

The field example does not require a spatial low-frequency model interpolated from well logs. However, the available well information contributed to wavelet estimation and to the broad AI range of the linear background used for comparison; it was not used directly to select the parameters of the four primary inversion schemes. The additional Bayesian comparators have the

separate reference-based calibration described above. This example therefore represents limited-well application rather than a fully well-independent or blind validation.

Figure 26 assesses seismic reconstruction for the four schemes in Figure 25a–d. The correlation coefficients for linear-single, LFD-single, linear-multi, and LFD-multi are 0.858, 0.858, 0.886, and 0.894, respectively, while the corresponding relative error energies are 28.36%, 28.36%, 22.90%, and 21.28%. LFD-multi thus gives the highest correlation and lowest reconstruction error among these four schemes. Compared with linear-multi, its error energy is 1.62 percentage points lower, indicating an additional improvement beyond the benefit of multi-trace coupling. The representative waveform comparison in Figure 26c is consistent with this improved data fit. These metrics refer to agreement with recorded seismic data, not independent absolute-impedance accuracy, and do not include the two Bayesian results in Figure 25e and 25f.

7. Limitations, uncertainties, and potential pitfalls

Broadband acquisition and processing are not prerequisites for applying the Laplace–Fourier transform, but they strongly affect the reliability of low-frequency AI estimation. Without them, conventional records may contain little usable energy at the lowest frequencies, and aggressive filtering, phase errors, or amplitude distortions may further weaken the constraints. A non-zero damped spectrum must not be interpreted as a direct measurement of a missing frequency band.

The resulting AI depends on damping and frequency

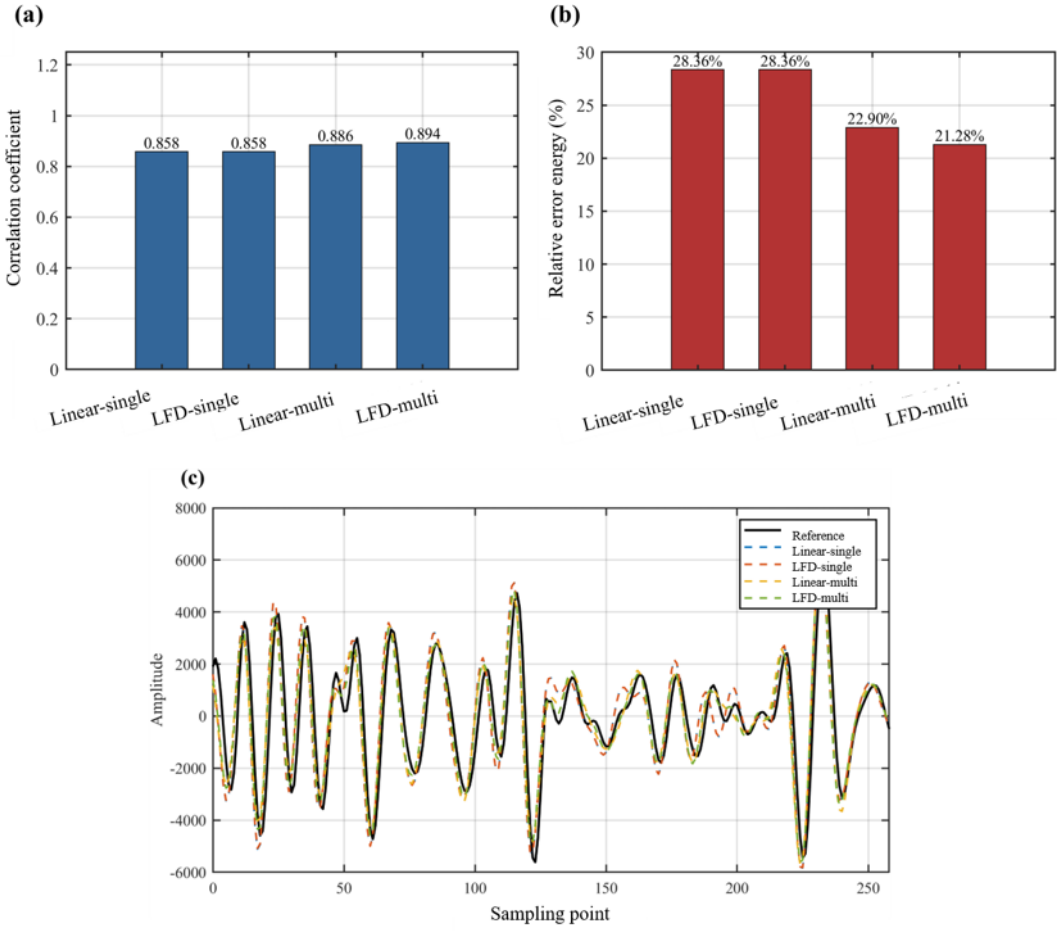


Figure 26. Field seismic-reconstruction assessment for linear-single, LFD-single, linear-multi, and LFD-multi: (a) correlation coefficients; (b) relative error energy; (c) representative recorded and reconstructed seismic traces. Methods are identified by the axis labels and legend. The metrics measure seismic-data fit, not independent absolute-impedance accuracy; the Bayesian results in Figure 25e and 25f are not included.
Abbreviation: LFD: Laplace–Fourier domain.

sampling, wavelet accuracy, noise, regularization, and the background-scale assumptions. Strong damping suppresses late-time samples and can reduce sensitivity to deeper structure; weak damping may provide little separation from conventional Fourier-domain inversion. Sparse and lateral constraints can stabilize the solution. Agreement with seismic data alone does not establish a unique absolute AI model or independently verified thin-bed thickness.

When conventional data provide insufficient low-frequency constraints and broadband acquisition or processing is unavailable, a conventional AI inversion with a transparently constructed well-derived or geological low-frequency model is preferable if such information is available. The proposed method can then serve as a complementary estimate and be checked against that baseline. If neither reliable low-frequency data nor a defensible background constraint is available, uncertainty in absolute AI must be retained rather than hidden by regularization.

8. Conclusion

This study presents a sparse multi-channel simultaneous inversion method based on the Laplace frequency domain. This method utilizes the Laplace frequency domain to extract the low-frequency information from seismic data, and further constructs a multi-channel inversion framework incorporating sparse regularization constraints, which is used to achieve high-precision estimation of AI. Furthermore, the selection of an appropriate Laplace damping factor is critical for retrieving deep low-frequency structural information, particularly in scenarios where insufficient prior geophysical knowledge hampers the construction of reliable low-frequency initial models. Under such conditions, inversion in the LFD effectively alleviates the dependence on the initial model. Furthermore, total variation regularization constrains lateral correlations among adjacent seismic traces, preserving stratigraphic boundaries and discontinuities while suppressing noise and improving the accuracy and stability of the inversion. Both synthetic and field data examples show that the proposed method yields robust, reliable AI estimates that can serve as high-quality, low-frequency background models for subsequent inversion, validating the feasibility and effectiveness of the approach.

An extension to elastic impedance inversion is a direction for future work. It would require an appropriate angle-dependent elastic forward model, suitable pre-stack observations, and explicit treatment of parameter coupling and identifiability. The present post-stack AI examples do not validate that extension.

Acknowledgments

None.

Funding

None.

Conflict of interest

The authors declare that they have no known competing financial interests or personal relationships that could have appeared to influence the work reported in this paper.

Author contributions

Conceptualization: Guangzhao Guo
Formal analysis: Guangzhao Guo
Investigation: Yuqiang Zhang
Methodology: Yuqiang Zhang
Supervision: Kai Lin
Writing–original draft: Guangzhao Guo
Writing–review & editing: Kai Lin, Xiaotao Wen, Lian Zhao

Ethics approval and consent to participate

Not applicable.

Consent for publication

Not applicable.

Availability of data

The theoretical model data and code used in this study can be obtained from the corresponding author upon reasonable request.

AI tools statement

No Al tools were used during the research or manuscript preparation process.

References

1. Geng WH, Lu WK, Li JY, *et al*. Multitrace seismic impedance inversion with structure-oriented minimum entropy stabilizer. *IEEE Trans Geosci Remote Sens*. 2024;62:1-13.

   doi: 10.1109/TGRS.2024.3462797

2. Li K, Yin XY, Zong ZY. Bayesian seismic multi-scale inversion in complex Laplace mixed domains. *Pet Sci*. 2017;14(4):510-517.

   doi: 10.1007/s12182-017-0191-0

3. Ampilov YP, Vladov ML, Tokarev MY. Broadband marine seismic acquisition technologies: challenges and opportunities. *Seism Instrum*. 2019;55(4):388-403.

   doi: 10.3103/S0747923919040030

4. Gao SH, Xue B, Lin Z, Chen Y, Zhu XY. High-resolution data

acquisition technique in broadband seismic observation systems. *Sci China Technol Sci*. 2016;59(6):961-972.

doi: 10.1007/s11431-016-6057-7

5. Chen Z, Haykin S. On different facets of regularization theory. *Neural Comput*. 2002;14(12):2791-2846.

doi: 10.1162/089976602760805296

6. Zhang YQ, Wen XT, Wu H, Liu J, Liu Y. Ji yu Lp ni fan shu xi shu yue shu he jiao ti fang xiang cheng zi suan fa de bo zu kang fan yan [Seismic impedance inversion based on Lp quasi-norm sparse constraint and alternating direction method of multipliers]. *Geophys Prospect Pet*. 2022;61(5):856-864. [In Chinese].

doi: 10.3969/j.issn.1000-1441.2022.05.010

7. Zhang TY, Lin K, Wen XT, Zhao L, Zhang YQ, Lei Y. Ying yong Lp ni fan shu xi shu yue shu de zong heng bo su bi zhi jie fan yan [Direct inversion of P- and S-wave velocity ratio with Lp quasi-norm sparse constraint]. *Oil Geophys Prospect*. 2024;59(2):230-237. [In Chinese].

doi: 10.13810/j.cnki.issn.1000-7210.2024.02.005

8. Zhao Y, Wen XT, Xie CL, Li B, Pan X, Zhou XY. Seismic inversion of anisotropic and isotropic fluid indicators and fracture density in the TTI medium. *IEEE Trans Geosci Remote Sens*. 2025;63:1-21.

doi: 10.1109/TGRS.2025.3563176

9. Sun QH, Zong ZY. AVO inversion for low-frequency component of the model parameters based on dual-channel convolutional network. *IEEE Trans Geosci Remote Sens*. 2023;61:1-14.

doi: 10.1109/TGRS.2023.3333341

10. Zhang HR, Yang P, Liu Y, Luo YN, Xu JY. Deep learning-based low-frequency extrapolation and impedance inversion of seismic data. *IEEE Geosci Remote Sens Lett*. 2022;19:1-5.

doi: 10.1109/LGRS.2021.3123955

11. Jin YC, Hu WY, Wang SR, Zi Y, Wu XQ, Chen JF. Efficient progressive transfer learning for full-waveform inversion with extrapolated low-frequency reflection seismic data. *IEEE Trans Geosci Remote Sens*. 2022;60:1-10.

doi: 10.1109/TGRS.2021.3129810

12. Shin CS, Cha YH. Waveform inversion in the Laplace domain. *Geophys J Int*. 2008;173(3):922-931.

doi: 10.1111/j.1365-246X.2008.03768.x

13. Shin CS, Cha YH. Waveform inversion in the Laplace-Fourier domain. *Geophys J Int*. 2009;177(3):1067-1079.

doi: 10.1111/j.1365-246X.2009.04102.x

14. Ha WS, Shin CS. Laplace-domain full-waveform inversion of seismic data lacking low-frequency information. *Geophysics*. 2012;77(5):199-206.

doi: 10.1190/geo2011-0411.1

15. Ha WS, Shin CS. Why do Laplace-domain waveform inversions yield long-wavelength results. *Geophysics*. 2013;78(4):167-173.

doi: 10.1190/geo2012-0365.1

16. Hu Y, Zhang D, Yuan JZ, *et al*. An efficient multi-scale waveform inversion method in Laplace-Fourier domain. *Pet Explor Dev*. 2015;42(3):369-378.

doi: 10.1016/S1876-3804(15)30027-6

17. Li K, Yin XY, Zong ZY. Pre-stack Bayesian cascade AVA inversion in complex-Laplace domain and its application to the broadband data acquired at East China. *J Pet Sci Eng*. 2017;158:751-765.

doi: 10.1016/j.petrol.2017.09.005

18. Cheng GS, Yin XY, Zong ZY, Liu J. Nonlinear elastic impedance inversion in Laplace-Fourier domain. *IEEE J Sel Top Appl Earth Obs Remote Sens*. 2019;12(11):4655-4663.

doi: 10.1109/JSTARS.2019.2950541

19. Meng X, Liu SX, Xu Y, Fu L. Application of Laplace domain waveform inversion to cross-hole radar data. *Remote Sens (Basel)*. 2019;11(16):1839.

doi: 10.3390/rs11161839

20. Huang L, Chen B, Pan XP, Wang P, Zhang GZ, Liu JX. Bayesian seismic azimuth-difference inversion of horizontal transversely isotropic media for low-frequency component of fracture weaknesses in Laplace-Fourier domain. *IEEE Trans Geosci Remote Sens*. 2022;60:1-8.

doi: 10.1109/TGRS.2022.3206918

21. Li L, Zhang GZ, Wang YJ, Hu GM. Joint Laplace- and Fourier-domain seismic inversion for orthorhombic medium parameter estimates. *IEEE Trans Geosci Remote Sens*. 2024;62:1-10.

doi: 10.1109/TGRS.2024.3355216

22. Rudin LI, Osher S, Fatemi E. Nonlinear total variation based noise removal algorithms. *Physica D*. 1992;60(1-4):259-268.

doi: 10.1016/0167-2789(92)90242-F

23. Zhang P, Han LG, Lu ZW, Shang XJ, Zhang DH. A robust source wavelet phase inversion method based on correlation norm waveform inversion. *IEEE Geosci Remote Sens Lett*. 2023;20:1-5.

doi: 10.1109/LGRS.2023.3316352

24. Zhao L, Lin K, Wen XT, Zhang YQ. The 3-D global prestack seismic inversion in the time-frequency mixed domain. *IEEE Trans Geosci Remote Sens*. 2023;61:1-15.

doi: 10.1109/TGRS.2023.3282250

25. Zhao L, Cao DP, Zhang YQ, An ZD, Lin K, Wen XT. Alternate iterative inversion of acoustic impedance and wavelet based on sparse constraints. *IEEE Trans Geosci Remote Sens*. 2025;63:1-12.

doi: 10.1109/TGRS.2025.3530566

26. Bohra P, Unser M. Continuous-domain signal reconstruction. *IEEE Trans Signal Process*. 2020;68:4543-4554.

    doi: 10.1109/TSP.2020.3013781

27. Sun JJ, Li YG. Adaptive Lp inversion for simultaneous recovery of both blocky and smooth features in a geophysical model. *Geophys J Int*. 2014;197(2):882-899.

    doi: 10.1093/gji/ggu067

28. Zhao L, Lin K, Wen XT, Zhang YQ. Anisotropic total variation pre-stack multitrace inversion based on Lp norm constraint. *J Pet Sci Eng*. 2023;220:111212.

    doi: 10.1016/j.petrol.2022.111212

29. Anagaw AY, Sacchi MD. Full waveform inversion with total variation regularization. In: *Recovery—2011 CSPG CSEG CWLS Convention*. Calgary, AB, Canada: Canadian Society of Exploration Geophysicists; 2011. Accessed November 18, 2026. https://geoconvention.com/wp-content/uploads/abstracts/2011/131-Full_Waveform_Inversion.pdf

30. Gholami A. Nonlinear multichannel impedance inversion by total-variation regularization. *Geophysics*. 2015;80(5):R217-R224.

    doi: 10.1190/geo2015-0004.1

31. Zhou DY, Yin XY, Zong ZY. Multi-trace basis-pursuit seismic inversion for resolution enhancement. *Geophys Prospect*. 2019;67(3):519-531.

    doi: 10.1111/1365-2478.12752

32. Cheng L, Wang SX, Li SJ, Ji YZ. Multi-trace nonstationary sparse inversion with structural constraints. *Acta Geophys*. 2020;68(3):675-685.

    doi: 10.1007/s11600-020-00430-3

33. Lin K, Zhao L, Wen XT, Zhang YQ. Time-frequency mixed domain multi-trace simultaneous inversion method. *GeoEnergy Sci Eng*. 2023;230:212164.

    doi: 10.1016/j.geoen.2023.212164

34. Sun T, Jiang H, Cheng LZ, Zhu W. Iteratively linearized reweighted alternating direction method of multipliers for a class of nonconvex problems. *IEEE Trans Signal Process*. 2018;66(20):5380-5391.

    doi: 10.1109/TSP.2018.2868269

35. Erseghe T, Zennaro D, Dall'Anese E, Vangelista L. Fast consensus by the alternating direction multipliers method. *IEEE Trans Signal Process*. 2011;59(11):5523-5537.

    doi: 10.1109/TSP.2011.2162831

36. Boyd S, Parikh N, Chu E, Peleato B, Eckstein J. Distributed optimization and statistical learning via the alternating direction method of multipliers. *Found Trends Mach Learn*. 2011;3(1):1-122.

    doi: 10.1561/2200000016

Appendix

To solve **Equation A1**, the ADMM framework was employed to partition the objective function into multiple sub-problems with individual constraints:

$$J(L)=\min_{L} Y'-G'L'D'L_2^2+\beta L-L_{02}^2+\gamma\left(d_{x1}^1+d_{y1}^1\right)+\lambda\left(d_x-LD_x+C_{x2}^2+d_y-D_yL+C_{y2}^2\right) \tag{A1}$$

$$J(d_x)=\min_{d_x}\gamma d_{x1}^1+\lambda d_x-LD_x+C_{x2}^2 \; s.t. d_x=LD_x \tag{A2}$$

$$J(d_y)=\min_{d_y}\gamma d_{y1}^1+\lambda d_y-D_yL+C_{y2}^2 \; s.t. d_y=D_yL \tag{A3}$$

$$J(C_x)=\min_{C_x} d_x-LD_x+C_{x2}^2 \tag{A4}$$

$$J(C_y)=\min_{C_y} d_y-D_yL+C_{y2}^2 \tag{A5}$$

Following Gholami,[30] the model-update equation is addressed by incorporating a 2D Sylvester equation, formulated as:

$$AX+XB=C \tag{A6}$$

Transforming **Equation A1** into the structure of **Equation A6** yields:

$$X=L \tag{A7}$$

$$A=\alpha\left(G'L'D'\right)^T G'L'D'+\beta E+\lambda D_y^T D_y \tag{A8}$$

$$B=\lambda D_x D_x^T \tag{A9}$$

$$C=\alpha\left(G'L'D'\right)^T Y+\lambda\left[D_y^T\left(d_y-C_y\right)+\left(d_x-C_x\right)D_x^T\right]+\beta L_0 \tag{A10}$$

where E denotes the identity matrix.

The optimization involving mixed L_1 and L_2 norms in **Equations A2** and **A3** is solved using the soft-threshold shrinkage operator in the standard proximal form.[36]

$$d_x=\max\left(\left|LD_x+C_x\right|-\left(\frac{\gamma}{\lambda}\right),0\right)\cdot\lambda sign\left(LD_x+C_x\right) \tag{A11}$$

$$d_y=\max\left(\left|D_yL+C_y\right|-\left(\frac{\gamma}{\lambda}\right),0\right)\cdot\lambda sign\left(D_yL+C_y\right) \tag{A12}$$

Here,

$$sign(a_i)=\begin{cases}1 & a_i>0\\ 0 & a_i=0\\ -1 & a_i<0\end{cases} \tag{A13}$$

For **Equations A4** and **A5**, which are characterized by L_2 norms, the gradients with respect to C_x and C_y are derived as follows:

$$C_x=LD_x-d_x \tag{A14}$$

$$C_y=D_yL-d_y \tag{A15}$$